



# Large eddy simulation/probability density function simulations of the Cambridge turbulent stratified flame series

Hasret Turkeri<sup>a,\*</sup>, Xinyu Zhao<sup>a</sup>, Stephen B. Pope<sup>b</sup>, Metin Muradoglu<sup>c</sup>

<sup>a</sup> Department of Mechanical Engineering, University of Connecticut, Storrs, CT 06269, USA

<sup>b</sup> Sibley School of Mechanical and Aerospace Engineering, Cornell University, Ithaca, NY, 14853, USA

<sup>c</sup> Department of Mechanical Engineering, Koc University, Rumelifeneri Yolu, Sariyer, Istanbul 34450, Turkey

## ARTICLE INFO

### Article history:

Received 17 July 2018

Revised 10 October 2018

Accepted 11 October 2018

Available online 24 October 2018

### Keywords:

LES/PDF method

Cambridge Stratified Flame

Bluff body stabilized

Premixed and stratified turbulent flames

## ABSTRACT

The LES/PDF methodology is applied to the Cambridge/Sandia turbulent stratified flame series. The methane chemistry is represented by the 16-species reduced ARM1 mechanism, and the *in situ* adaptive tabulation method is adopted to accelerate the chemistry calculations. Differential diffusion effects are taken into account. The simulations are performed for premixed (SwB1), and moderately and highly stratified (SwB5 and SwB9, respectively) cases under non-swirling conditions. The results from LES/PDF simulations are compared with the experimental measurements and with previous calculations. The calculated length of the recirculation zone, the mean and r.m.s. profiles of velocity, temperature, equivalence ratio and mass fractions of species are in very good agreement with the measurements. In the stratified cases, the CO profiles are underestimated within the recirculation zone, close to the bluff body. Scatter plots of species mole fractions and temperature are presented and compared with the experimental data. Conditional means of species mass fractions demonstrate overall good consistency with the measurements. A parametric study is then performed to examine the effect of differential diffusion and the effect of the parameter controlling the scalar mixing rate. It is found that differential diffusion has a negligible effect on the mean and r.m.s. results, whereas, the mixing rate parameter has a considerable effect on the flow structure. Finally, the effect of stratification is investigated and characterized by scatter plots of OH mass fraction and heat release rate (HRR) in the equivalence ratio space.

© 2018 The Combustion Institute. Published by Elsevier Inc. All rights reserved.

## 1. Introduction

In practical combustion devices, the limited time and length scales imposed by design constraints may prevent the fuel from mixing perfectly with the oxidizer (e.g., in gas turbines [1]). The fuel concentration can vary spatially within the combustion chamber, which leads to the partially premixed or the stratified combustion, i.e., the flame front propagates through an inhomogeneous mixture composition. Additionally, the stratification in fuel concentrations may exist intentionally for design purposes to increase the flame stability for lean combustion (e.g., in direct-injection spark ignition (DISI) engines [2]). Due to the practical relevance of stratified combustion, it has attracted increasing interest in recent years.

Stratified flames under laminar [3–7], weakly turbulent [8–12] and strongly turbulent conditions [13–18] have been extensively investigated in the literature. The difference between a stratified flame and a homogeneously-mixed premixed flame is a common

interest among these studies. Experimental and numerical studies of laminar stratified flames [3–7] report enhancement in the flammability limits and reaction rates, compared to homogeneously-mixed flames. The enhancement is attributed to the enrichment of radicals and enthalpy provided by the “back-support” stratified mixtures. The displacement speed of the stratified flame depends not only on the local equivalence ratio but also on the history of the stratified flame propagation [19]. Similarly, increased flame speeds [9], enhanced flammability limits [12], and higher flame surface densities [11] are also observed for low Reynolds number stratified flames. For stratified flames with high Reynolds numbers, the flame surface density and the scalar dissipation rates are not significantly altered by the stratification, while the probability density functions of the curvature are slightly broadened [17,18]. Lastly, differential diffusion is speculated to play a significant role in modifying the local burning rate in stratified combustion [20]. Barlow et al. [21] have studied the effect of the differential diffusion on the Cambridge/Sandia swirl burner. They have reported non-conserved atom ratios across the flame brush, which is attributed to the effect of differential diffusion.

\* Corresponding author

E-mail address: [hasretturkeri@gmail.com](mailto:hasretturkeri@gmail.com) (H. Turkeri).

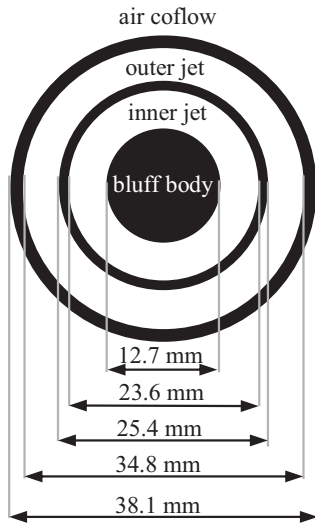


Fig. 1. A schematic of the stratified bluff body burner.

A comprehensive review on stratified flames and associated modeling studies can be found in [20].

Various numerical models for stratified turbulent combustion have been proposed in the literature [22–28]. Validation of the numerical models requires well-characterized benchmark test cases. The Darmstadt stratified burner designed by Dreizler et al. [15,16] and the Cambridge/Sandia swirl burner designed by Sweeney et al. [17,18] have become platforms for studying highly turbulent stratified flows [29]. The Darmstadt burner has been used to study the effect of the shear and stratification in moderate and intense turbulence. The burner consists of three slots surrounded by an air coflow and the flame is stabilized by a pilot flame fed through a central slot, in which the flow configuration is relatively simple. The Cambridge/Sandia swirl burner provides more complex and thus complementary cases to those obtained from the Darmstadt burner. The Cambridge/Sandia swirl burner is designed to investigate the effect of stratification under swirling and non-swirling conditions. It consists of a central bluff body and two fuel streams surrounded by an air coflow. The flame is stabilized by a recirculation behind the bluff body. The two annular jets inject fuel/air mixtures at different equivalence ratios. Different combustion models have been applied to the Darmstadt stratified flames series. A thickened flame model by Kuenne et al. [22] and Ketelheun et al. [23], the G-equation model by Trisjono et al. [24] and the fractal closure model by Cavallo et al. [25] have been used to simulate the Darmstadt stratified flames series. The Cambridge turbulent stratified flame series under non-swirl conditions have previously been studied numerically by Nambully et al. [27,30] using a filtered-laminar-flame PDF model, by Proch and Kempf [26] using an artificial thickened flame model, and by Brauner et al. [28] using a PDF model based on the Eulerian stochastic field method in which the PDF is represented by an ensemble of stochastic fields for each scalars. In all the previous LES studies, the flow fields and the species profiles have been predicted quite accurately, except for the CO profiles. The numerical predictions for CO show apparent discrepancies close to the bluff body in the stratified cases. Mercier et al. [31] have studied the effect of heat loss through the bluff body using a sub-grid scale (SGS) flame wrinkling models in the context of the filtered tabulated chemistry formulation (FTC). There heat loss is found to affect the temperature profiles significantly. More recently, flame-resolved DNS of the Cambridge stratified flame series is reported [32], where the

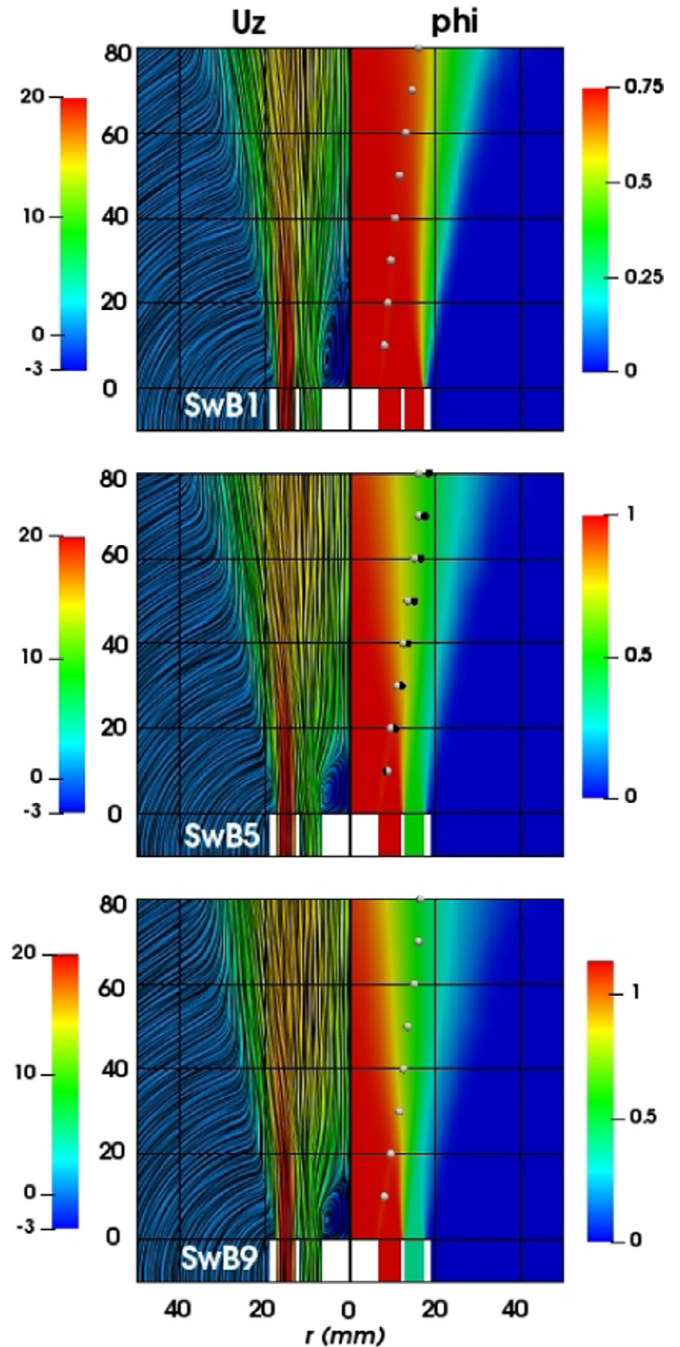
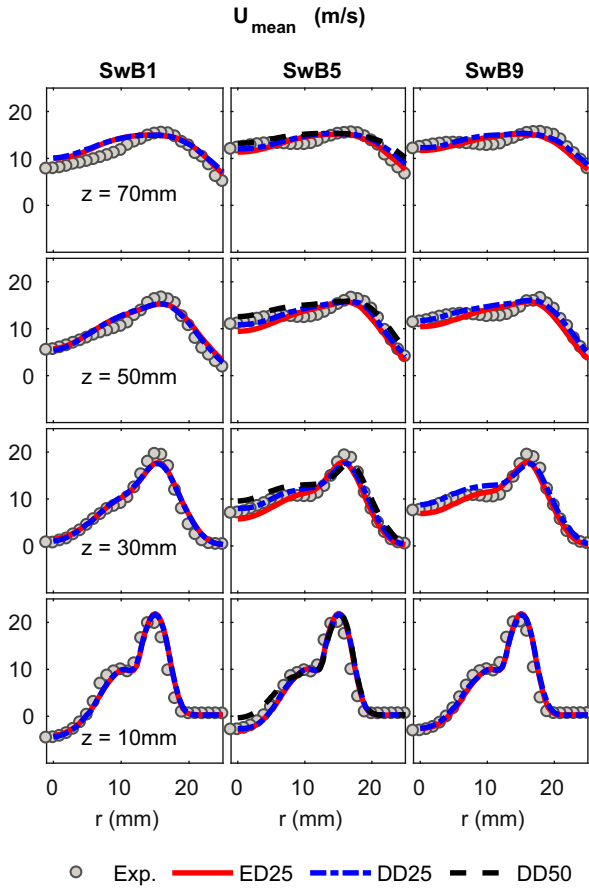


Fig. 2. The mean axial velocity superimposed by time-averaged streamlines (left), and the mean equivalence ratio (right), from Model DD25. The white and black points (only in SwB5) indicate the locations of the flame fronts from Model DD25 and Model DD50, respectively. .

flame thickness and the Kolmogorov scales are resolved within the flame zone. The prediction of the r.m.s. velocities and the CO profiles are much improved, compared to their previous LES studies. However, discrepancies between the experiments and the simulations can still be observed.

The main goal of the present computational study is to show the performance of the LES/PDF methodology employing the Lagrangian Monte Carlo method in numerical solutions for predicting the effects of stratification using the Cambridge turbulent stratified flame series. The PDF method has proven to be very



**Fig. 3.** Radial profiles of the mean resolved axial velocity at different axial locations. Symbols: experimental data; red solid line: Model ED25; blue dot dashed line: Model DD25; black dashed line: Model DD50. (For interpretation of the references to color in this figure legend, the reader is referred to the web version of this article).

successful in non-premixed [33–36], premixed [37–39] and partially premixed [40] combustion modes, because it involves few intrinsic assumptions regarding the mixture composition, the flame speed, the flame structures, and the flame topology. The highly non-linear chemical reaction source terms are treated exactly without requiring any modeling. The conditional diffusion terms remain in unclosed forms, hence need to be modeled by mixing models. In the context of LES, the results are less sensitive to the choice of mixing models, compared to those obtained by the RANS methodology. The interaction by exchange with the mean (IEM) model with mean drift terms [41] has proven to be very efficient to model the conditional diffusion term in several previous studies [39,42–44]. These characteristics of the PDF methods make it a suitable candidate to model stratified flames.

In the present study, a hierarchy of cases, including the premixed case, the moderately and highly stratified cases, is investigated using the LES/PDF method, for the non-swirling conditions. The rest of the paper is organized as follows. In Section 2, the governing equations and the numerical solution methodology for the LES/PDF method are presented. In Section 3, the details of the experimental setup and the numerical simulations are described, followed by results and discussions in Section 4. Finally, conclusions from the study are summarized in Section 5. A comparison of the present results with the previously-published results is presented in the Appendix.

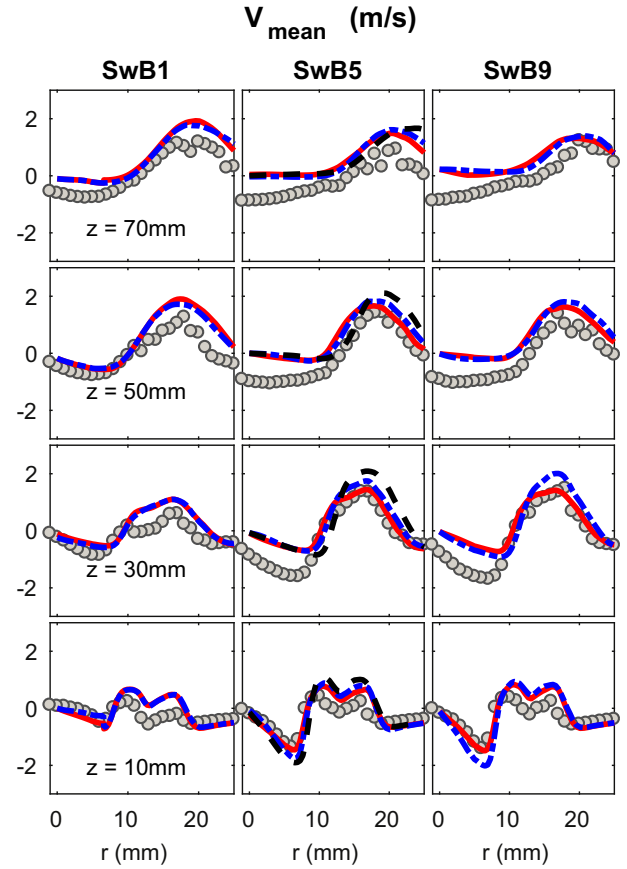


**Fig. 4.** Radial profiles of the mean resolved radial velocity at different axial locations. Symbols: experimental data; red solid line: Model ED25; blue dot dashed line: Model DD25; black dashed line: Model DD50. (For interpretation of the references to color in this figure legend, the reader is referred to the web version of this article).

## 2. Methodology

### 2.1. Governing equations

In the LES method, the fields in a turbulent reacting flow are separated into large (filtered or resolved) and small (subfilter or unresolved) scales by applying a low band-pass filtering operation: for instance, the filtered density field  $\bar{\rho}$  is defined as

$$\bar{\rho}(\mathbf{x}, t) \equiv \int_{-\infty}^{\infty} \rho(\mathbf{y}, t) G(\mathbf{y} - \mathbf{x}) d\mathbf{y}, \quad (1)$$

where  $\rho(\mathbf{x}, t)$  is the density field and  $G$  is the LES filter. Applying this filter to the instantaneous mass and momentum conservation equations, one obtains

$$\frac{\partial \bar{\rho}}{\partial t} + \frac{\partial \bar{\rho} \tilde{u}_i}{\partial x_i} = 0, \quad (2)$$

$$\frac{\partial \bar{\rho} \tilde{u}_i}{\partial t} + \frac{\partial \bar{\rho} \tilde{u}_i \tilde{u}_j}{\partial x_j} = -\frac{\partial \bar{p}}{\partial x_i} + \frac{\partial \tau_{ij}}{\partial x_j} + \frac{\partial T_{ij}}{\partial x_j}, \quad (3)$$

where  $\tilde{u}_j$  and  $\bar{p}$  are the Favre-filtered velocity and the filtered pressure fields, respectively. In Eq. (3), the resolved viscous stress tensor is modeled as

$$\tau_{ij} = \bar{\mu} \left( \frac{\partial \tilde{u}_i}{\partial x_j} + \frac{\partial \tilde{u}_j}{\partial x_i} - \frac{2}{3} \frac{\partial \tilde{u}_k}{\partial x_k} \delta_{ij} \right), \quad (4)$$

where  $\bar{\mu}$  is the molecular viscosity that is evaluated using the filtered compositional fields. The last term on the right hand

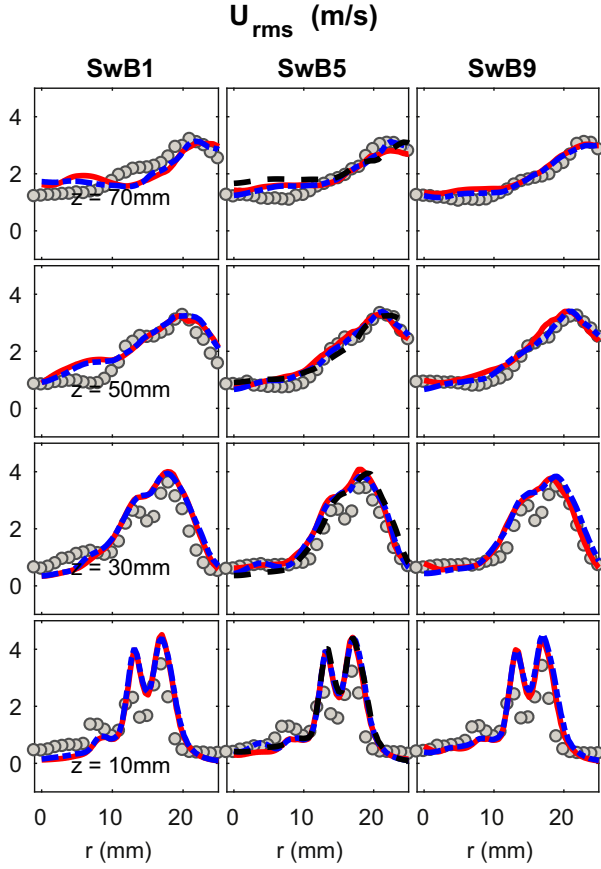


**Fig. 5.** Radial profiles of the r.m.s. of the resolved axial velocity at different axial locations. Symbols: experimental data; red solid line: Case ED25; blue dot dashed line: Model DD25; black dashed line: Model DD50. (For interpretation of the references to color in this figure legend, the reader is referred to the web version of this article).

side of Eq. (3) represents the unclosed subfilter stress tensor defined as  $T_{ij} = \bar{\rho} \tilde{u}_i \tilde{u}_j - \bar{\rho} \tilde{u}_i \tilde{u}_j$ , and it is modeled using the dynamic Smagorinsky model [45].

For variable density flows, the filtered mass density function (FMDf) of compositions [46,47] is defined as

$$\mathcal{F}(\boldsymbol{\psi}; \mathbf{x}, t) \equiv \int_{-\infty}^{\infty} \rho(\mathbf{y}, t) \delta(\boldsymbol{\psi} - \boldsymbol{\phi}(\mathbf{y}, t)) G(\mathbf{y} - \mathbf{x}) d\mathbf{y}, \quad (5)$$

where  $\boldsymbol{\phi}$  represents the  $N = N_s + 1$  compositional space consisting of the mass fractions of  $N_s$  species and the sensible enthalpy,  $\boldsymbol{\psi}$  is the sample space variable for the compositions and  $\delta$  is the  $N$ -dimensional delta function. The Favre-filtered PDF  $\tilde{f}$  is related to the FMDf as  $\tilde{f} = \mathcal{F}/\bar{\rho}$ . Then the Favre-filtered mean of a flow variable  $Q$  as a function of  $\boldsymbol{\phi}$  can be defined as

$$\tilde{Q}(\mathbf{x}, t) = \int Q(\boldsymbol{\psi}; \mathbf{x}, t) \tilde{f}(\boldsymbol{\psi}; \mathbf{x}, t) d\boldsymbol{\psi}. \quad (6)$$

The modeled transport equation for  $\tilde{f}$  can be written as [46,47]

$$\begin{aligned} & \frac{\partial \bar{\rho} \tilde{f}}{\partial t} + \frac{\partial \bar{\rho} \tilde{u}_i \tilde{f}}{\partial x_i} - \frac{\partial}{\partial x_i} \left( \bar{\rho} \tilde{D}_T \frac{\partial \tilde{f}}{\partial x_i} \right) \\ &= \frac{\partial}{\partial \psi_\alpha} \left[ \bar{\rho} \tilde{f} \Omega(\psi_\alpha - \tilde{\phi}_\alpha) \right] - \frac{\partial}{\partial \psi_\alpha} \left[ \tilde{f} \frac{\partial}{\partial x_i} (\bar{\rho} V_{\alpha,i}) \right] \\ & - \frac{\partial}{\partial \psi_\alpha} \left[ \bar{\rho} \tilde{f} S_\alpha(\boldsymbol{\psi}) \right]. \end{aligned} \quad (7)$$

The last two terms on the left-hand side of Eq. (7) represent the change of  $\tilde{f}$  in the physical space due to convection by the filtered

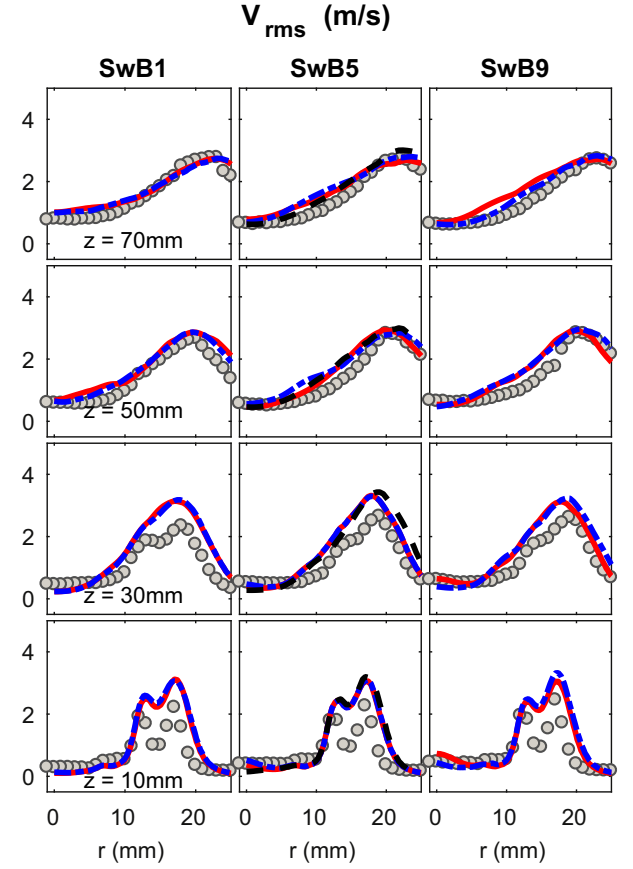


**Fig. 6.** Radial profiles of the r.m.s. of the resolved radial velocity at different axial locations. Symbols: experimental data; red solid line: Case ED25; blue dot dashed line: Model DD25; black dashed line: Model DD50. (For interpretation of the references to color in this figure legend, the reader is referred to the web version of this article).

velocity  $\tilde{u}_i$  and to turbulent diffusion with diffusivity  $\tilde{D}_T$ . The first two terms on the right-hand side represent the transport of  $\tilde{f}$  in the composition space due to the molecular mixing and transport, where  $V_{\alpha,i}$  is a corrected diffusion velocity related to the mixture-averaged molecular diffusivity,  $\tilde{D}_{(\alpha)}$ , of species  $\alpha$  or the thermal diffusivity for the sensible enthalpy. The mixing term is modeled by the IEM mixing model and the transport term is represented by a mean drift term [41]. The corrected diffusion velocity is defined as

$$V_{\alpha,i} = \begin{cases} \tilde{D}_{(\alpha)} \frac{\partial \tilde{\phi}_\alpha}{\partial x_i} - \tilde{\phi}_\alpha \tilde{D}_\beta \frac{\partial \tilde{\phi}_\beta}{\partial x_i} & \text{for species } \alpha, \\ \tilde{D}_{(\alpha)} \frac{\partial \tilde{\phi}_\alpha}{\partial x_i} & \text{for enthalpy,} \end{cases} \quad (8)$$

where suffices in parentheses are excluded from the summation convention, which otherwise applies to composition indices (here  $\alpha$  and  $\beta$ ). In Eq. (8-first line) the first term is the mean drift term for each species and the second term is the correction velocity to satisfy the mass conservation in case of differential diffusion. This implementation of molecular transport does not give rise to the spurious production of scalar variance and is able to account for the effects of differential diffusion in the mean drift term. For molecular mixing, the scalar mixing rate  $\Omega$  is modeled as

$$\Omega = C_m \frac{\tilde{D} + \tilde{D}_T}{\Delta^2}, \quad (9)$$

where  $\tilde{D}$  is thermal diffusivity,  $C_m$  is a model constant, and is determined based on sensitivity studies by matching the statistics from experiments.  $\Delta$  is the LES filter size that is defined as  $\sqrt[3]{\Delta V}$ ,

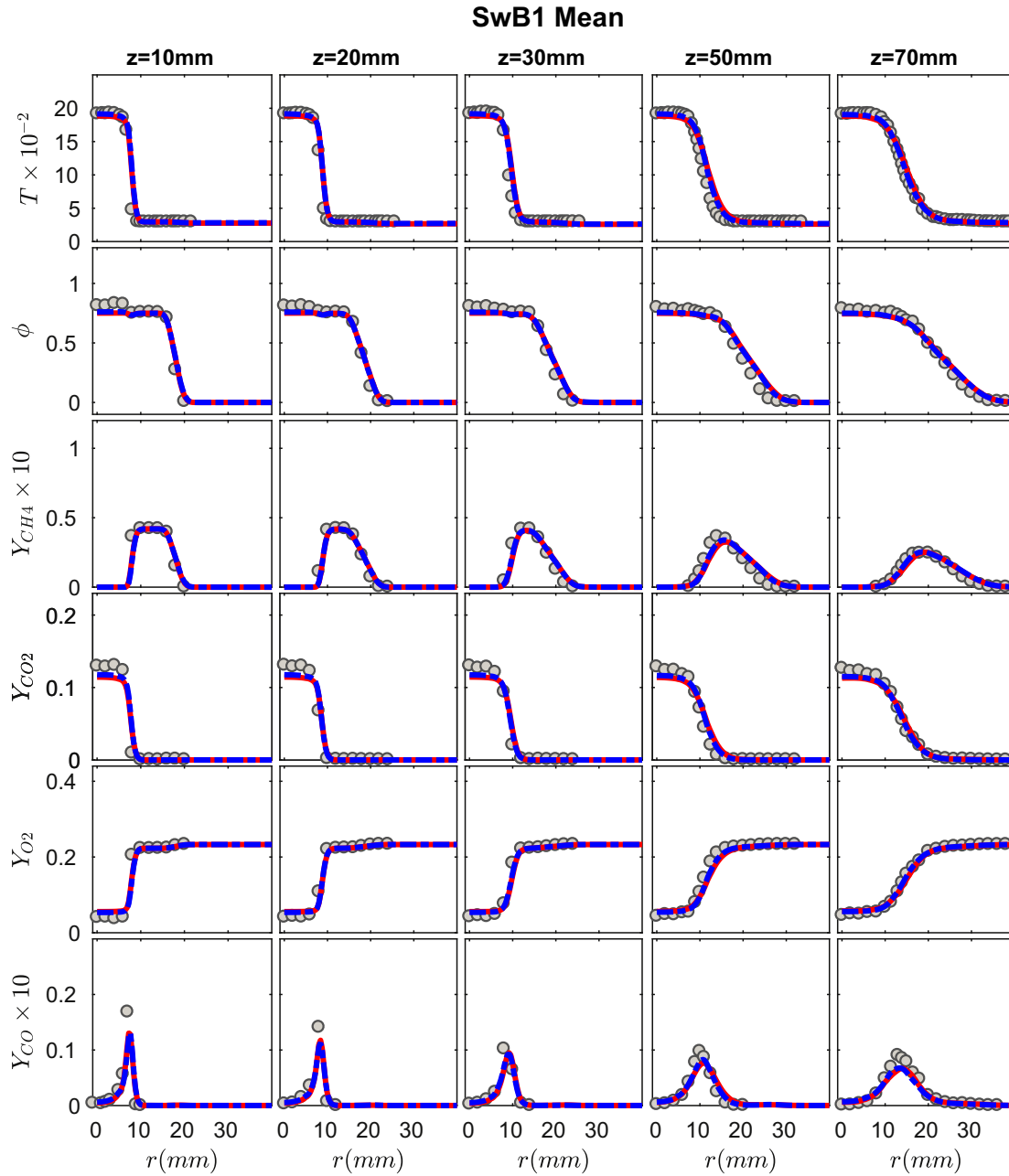


**Fig. 7.** SwB1: The radial profiles of the time-averaged resolved temperature and the resolved mass fractions of  $\text{CH}_4$ ,  $\text{CO}_2$ ,  $\text{O}_2$  and  $\text{CO}$  at five axial locations of  $z = 10, 20, 30, 50, 70$  mm. Symbols: experimental data; red solid line: Model ED25; blue dot dashed line: Model DD25. (For interpretation of the references to color in this figure legend, the reader is referred to the web version of this article).

where  $\Delta V$  is the volume of the computational grid cell. Here, the turbulent diffusivity  $\tilde{D}_T$  is obtained from the turbulent eddy viscosity concept as  $\tilde{\rho}\tilde{D}_T = \tilde{\mu}_T/Sc_t$  where  $Sc_t$  is the turbulent Schmidt number with a constant value of  $Sc_t = 0.4$  [48]. It should be noted that differential diffusion is not considered in the molecular mixing model.

Finally, the last term in Eq. (7) represents the evolution of  $\tilde{f}$  in the composition space due to chemical reactions, and it appears in closed form. In this study, the molecular viscosity  $\tilde{\mu}$ , and the thermal and species diffusivities,  $\tilde{D}_\alpha$  are evaluated using CHEMKIN's transport library, as functions of the resolved composition and resolved temperature.

## 2.2. The solution methodology for LES/PDF model equations

The filtered conservation of mass and momentum equations (Eqs. (2)–(3)) are solved numerically by the finite-volume method, and a Monte Carlo approach in the Lagrangian framework is adopted to obtain the numerical solution of the modeled transport equation for  $\tilde{f}$  (Eq. (7)) due to its high dimensionality. In the Lagrangian framework, the flow is represented by a large number of notional Lagrangian particles. The position and composition of the notional Lagrangian particles evolve by the following stochastic differential equations [41]:

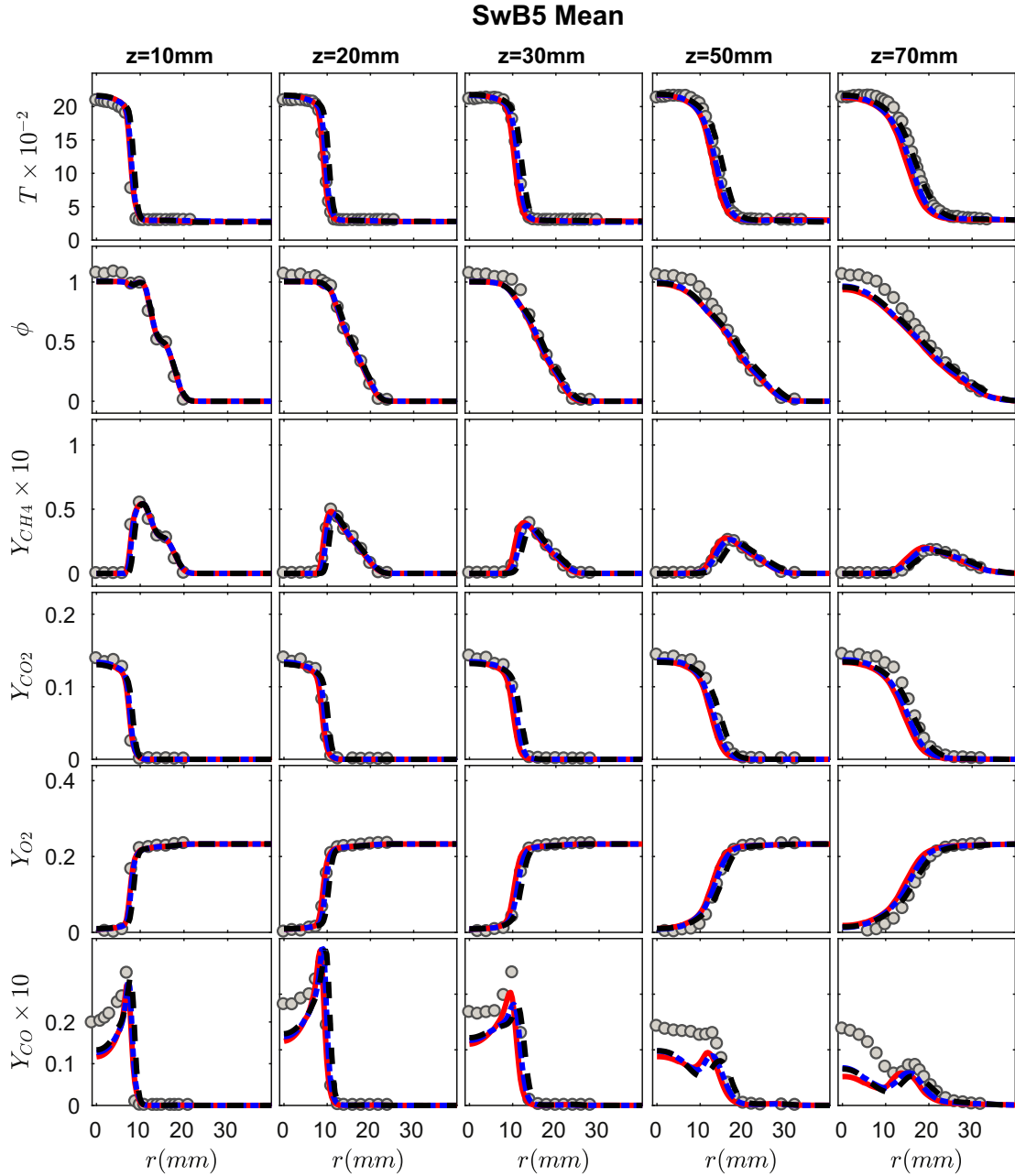


**Fig. 8.** SwB5: The radial profiles of the time-averaged resolved temperature and the resolved mass fractions of CH<sub>4</sub>, CO<sub>2</sub>, O<sub>2</sub> and CO at five axial locations of  $z = 10, 20, 30, 50, 70$  mm. Symbols: experimental data; red solid line: Model ED25; blue dot dashed line: Model DD25; black dashed line: Model DD50. (For interpretation of the references to color in this figure legend, the reader is referred to the web version of this article).

$$dX_j^* = \left( \tilde{u}_j + \frac{1}{\bar{\rho}} \frac{\partial(\bar{\rho}\tilde{D}_T)}{\partial x_j} \right)^* dt + (2\tilde{D}_T^*)^{1/2} dW_j^*, \quad (10)$$

$$\frac{d\phi_\alpha^*}{dt} = -\Omega^*(\phi_\alpha^* - \tilde{\phi}_\alpha^*) + \left[ \frac{1}{\bar{\rho}} \frac{\partial \bar{\rho} V_{\alpha,i}}{\partial x_i} \right]^* + S_\alpha(\phi^*), \quad (11)$$

where  $dW_j^*$  denotes the Wiener increment in the  $j$  direction. The superscript “\*” denotes the particle properties, or the LES fields evaluated at the particle locations.

The resulting solution methodology is a hybrid method composed of (i) an Eulerian finite-volume method for solving the filtered conservation equations for mass and momentum (referred to as the LES solver), and (ii) a Lagrangian Monte Carlo method for the modeled transport equations for the joint PDF of compositions (denoted as the PDF solver). For the hybrid LES/PDF approach, the

resolved velocity  $\tilde{u}_i$ , the turbulent viscosity  $\tilde{\mu}_T$ , the turbulent diffusivity  $\tilde{D}_T$  and the mixing frequency  $\Omega$  are calculated by the LES solver. The PDF solver advances the notional particles in the physical space and composition space, and provides the filtered density  $\bar{\rho}$ , the Favre-filtered temperature  $\tilde{T}$  and mass fractions  $\tilde{Y}_\alpha$  to the LES solver.

The filtered density  $\bar{\rho}$ , and the Favre filtered temperature  $\tilde{T}$  and mass fractions  $\tilde{Y}_\alpha$  are calculated at cell center locations from the particles using the cloud-in-cell (CIC) method [49]. The LES fields used in the particle equations (Eqs. (10) and (11)) are interpolated from the cell centers to the particle locations using linear basis functions [50].

The filtered density  $\bar{\rho}$  extracted from the particles contains significant noise because only a finite number of notional particles can be used to solve the stochastic equations. Therefore, the direct

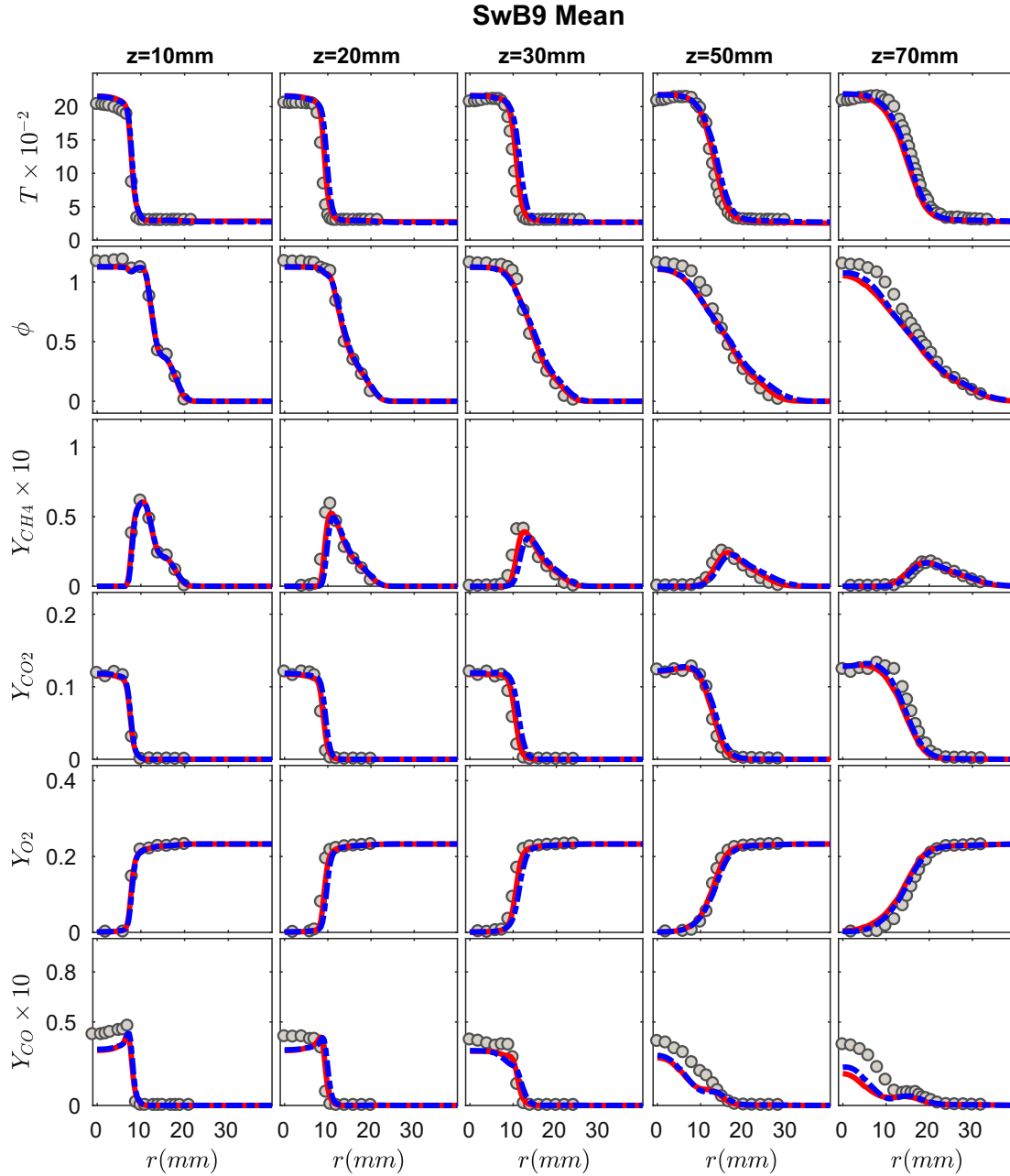


**Fig. 9.** SwB9: The radial profiles of the time-averaged resolved temperature and the resolved mass fractions of CH<sub>4</sub>, CO<sub>2</sub>, O<sub>2</sub> and CO at five axial locations of  $z = 10, 20, 30, 50, 70$  mm. Symbols: experimental data; red solid line: Model ED25; blue dot dashed line: Model DD25. (For interpretation of the references to color in this figure legend, the reader is referred to the web version of this article).

use of the filtered density  $\bar{\rho}$  from the particles in the LES solver is prone to cause significant numerical instabilities. To overcome this difficulty, the transported specific volume (TSV) method [51] is employed in this study. For the TSV method, instead of being directly obtained from the PDF solver, the filtered density  $\bar{\rho}$  to be used in the LES equations ((Eqs. 2–3)) is obtained from the solution of a transport equation for the Favre-filtered specific volume  $\tilde{v}$  as

$$\frac{\partial \bar{\rho} \tilde{v}}{\partial t} + \frac{\partial (\bar{\rho} \tilde{u}_j \tilde{v})}{\partial x_j} = \frac{\partial}{\partial x_j} \left( \bar{\rho} \tilde{D}_T \frac{\partial \tilde{v}}{\partial x_j} \right) + S_v + \dot{\omega}_v, \quad (12)$$

where  $S_v$  is received from the PDF solver and represents the change of Favre-filtered specific volume  $\tilde{v}$  due to the molecular mixing, the molecular diffusion, and chemical reactions. The last

term in Eq. (12) is a relaxation term of the form

$$\dot{\omega}_v = \bar{\rho} \frac{\tilde{v}_{PDF} - \tilde{v}}{\tau_v}, \quad (13)$$

where  $\tilde{v}_{PDF}$  is the specific volume obtained from the particles in the PDF solver and  $\tau_v$  is the relaxation time scale taken here as  $\tau_v = 4\Delta t$  with  $\Delta t$  being the time step. Once the specific volume is calculated from Eq. (12), the filtered density  $\bar{\rho}$  to be used in the LES equations is obtained as

$$\bar{\rho} = \frac{1}{\tilde{v}}. \quad (14)$$

To satisfy the boundedness condition imposed by the scalar transport in Eqs. (10) and (11), the *minimum-decay-factor adjustment* [41] is employed.

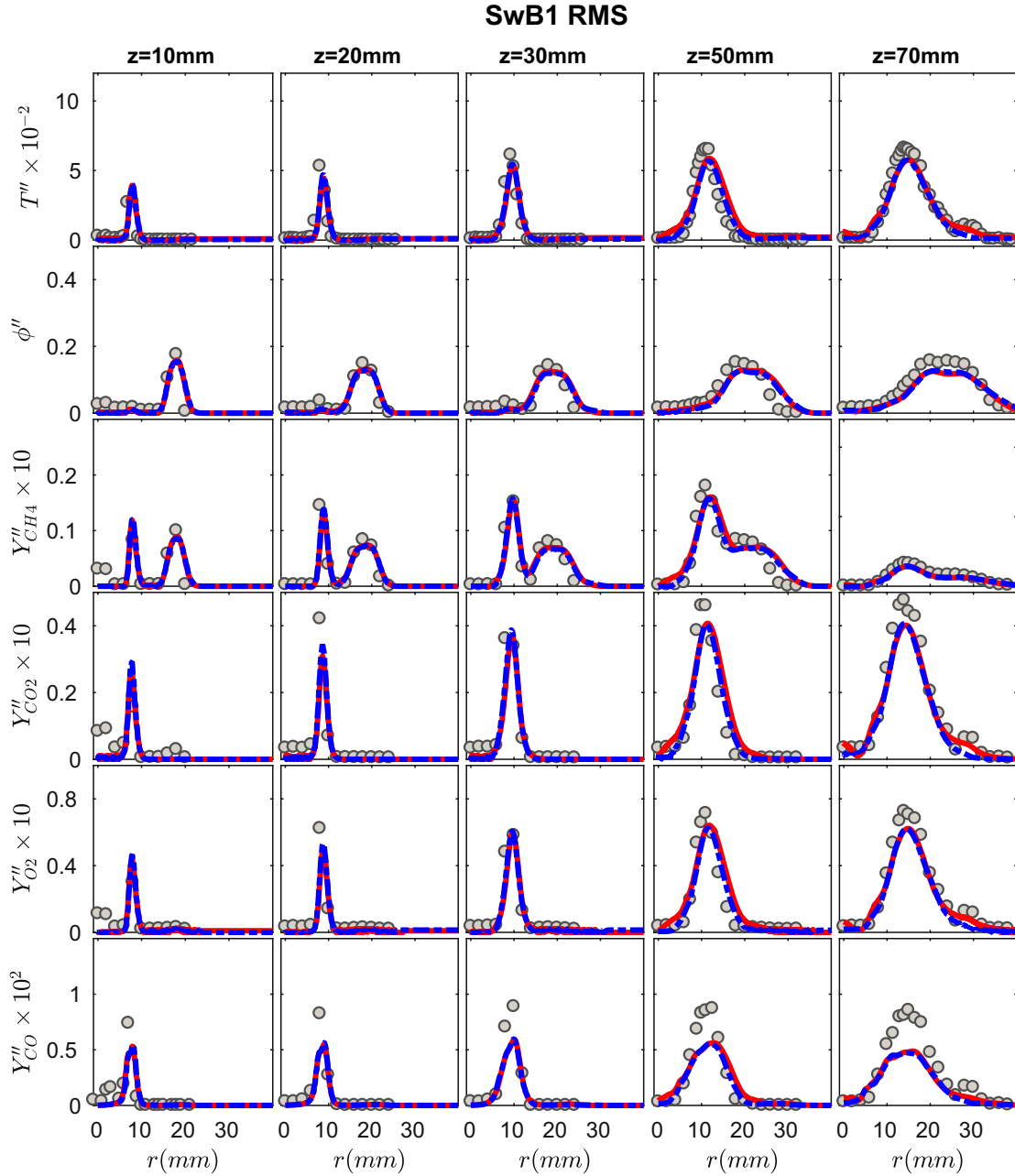


**Fig. 10.** SwB1: The radial profiles of the r.m.s. of temperature and the r.m.s. of mass fractions of  $\text{CH}_4$ ,  $\text{CO}_2$ ,  $\text{O}_2$  and  $\text{CO}$  at five axial locations of  $z = 10, 20, 30, 50, 70$  mm. Symbols: experimental data; red solid line: Model ED25; blue dot dashed line: Model DD25. (For interpretation of the references to color in this figure legend, the reader is referred to the web version of this article).

The *pdfFoam* solver [52] that is a LES/PDF solver on non-orthogonal hexahedral meshes and that is developed entirely within OpenFOAM is used to solve the modeled equations of the LES/PDF method described above. For the LES solver, second-order central differences are applied to approximate all spatial derivatives, except for the convection terms in the scalar equations (Eq. (12)) that are discretized using the SuperBee flux limiter [53] to avoid unphysical oscillations. A second-order backward differentiation scheme is used for the temporal discretization of all LES equations. The flow and scalar equations are solved sequentially. The pressure-velocity coupling is achieved using the PISO [54] method. For the PDF solver, the first-order fractional time scheme (TMR) [55] is used to advance particles in time. The cloud-in-cell (CIC) method is used to estimate the mean properties from the particles. To ensure the consistency between the LES and the

PDF solvers, the first two stages of the three-stage velocity correction algorithm described in [50] are employed. The *in situ* adaptive tabulation (ISAT) method [56,57] is used to accelerate the evaluation of the chemical source terms. More details of the *pdfFoam* solver can be found in [52].

### 3. Experimental configuration and simulation details

The Cambridge/Sandia swirl burner was designed to investigate the effect of stratification under swirl and non-swirl operating conditions. Here we consider only the non-swirl cases, and we will discuss the swirl cases in a subsequent study [58]. A schematic of the burner is shown in Fig. 1. The burner consists of a central bluff body surrounded by two annular fuel jets, i.e., the inner and the outer jets, outside of which an air coflow is supplied

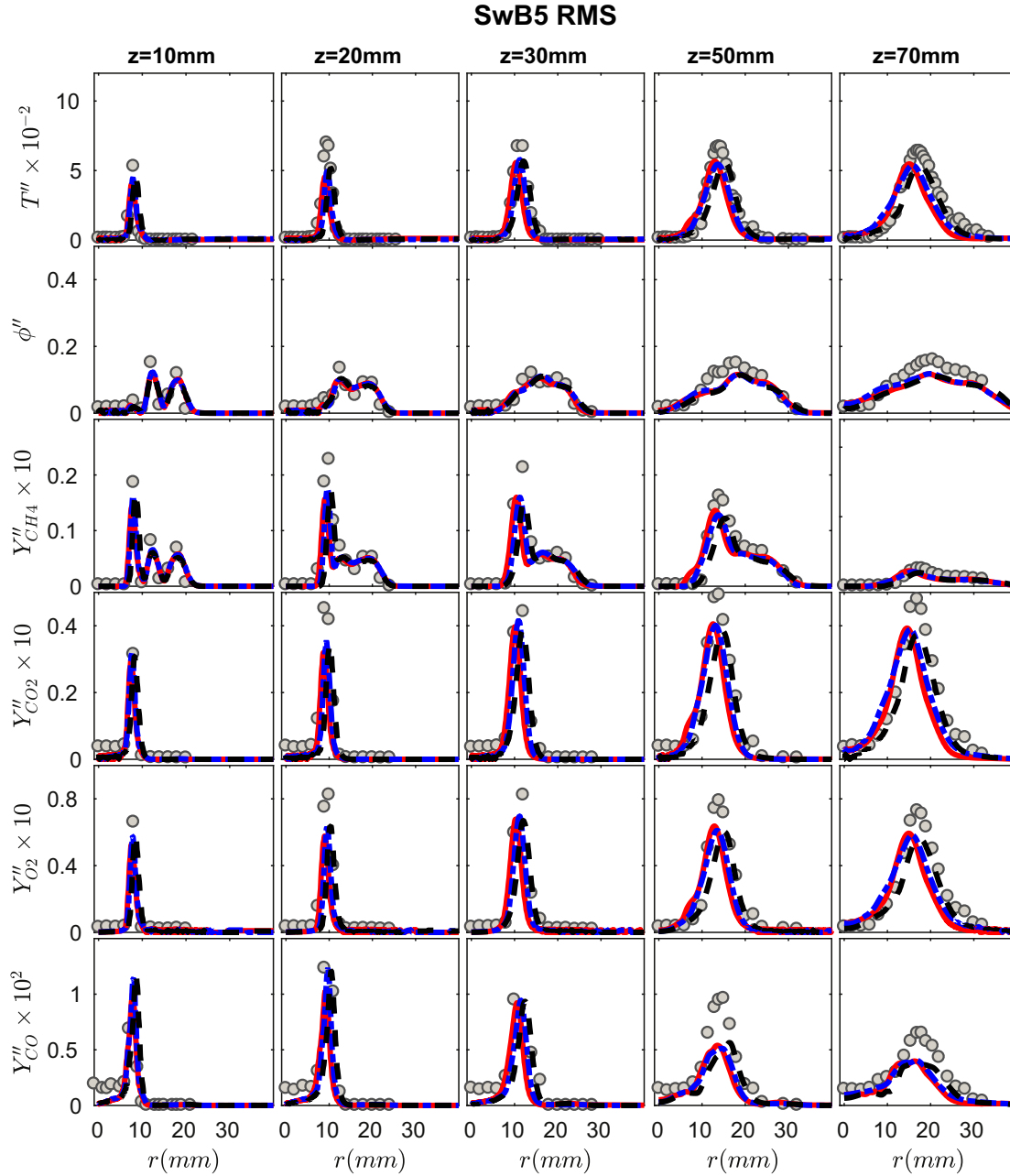


**Fig. 11.** SwB5: The radial profiles of the r.m.s. of temperature and the r.m.s. of mass fractions of  $\text{CH}_4$ ,  $\text{CO}_2$ ,  $\text{O}_2$  and  $\text{CO}$  at five axial locations of  $z = 10, 20, 30, 50, 70$  mm. Symbols: experimental data; red solid line: Model ED25; blue dot dashed line: Model DD25; black dashed line: Model DD50. (For interpretation of the references to color in this figure legend, the reader is referred to the web version of this article).

to reduce the entrainment of the ambient air. For the inner and outer jets, the inlet bulk velocities are 8.31 m/s and 18.7 m/s, corresponding to Reynolds numbers of 5960 and 11,500, respectively. The air coflow is laminar with an inlet velocity of 0.4 m/s. Three different stratification configurations, including premixed (SwB1), moderately stratified (SwB5), and highly stratified (SwB9) cases, are summarized in Table 1. There, following the experimental studies, the equivalence ratio ( $\phi$ ) is defined as

$$\phi = \frac{(X_{\text{H}_2} + X_{\text{H}_2\text{O}})/2 + X_{\text{CO}_2} + X_{\text{CO}} + 2X_{\text{CH}_4}}{X_{\text{O}_2} + X_{\text{CO}_2} + (X_{\text{H}_2\text{O}} + X_{\text{CO}})/2}, \quad (15)$$

where  $X_\alpha$  is the mole fraction of species  $\alpha$ . The stratification ratios, defined as the ratio of the equivalence ratios at the inner and outer jets ( $\phi_{\text{inner}}/\phi_{\text{outer}}$ ) for the cases of SwB5 and SwB9, are set as two and three, respectively, to investigate the effect of

**Table 1**  
Equivalence ratios of the two annular jets.

Case	$\phi_{\text{inner}}$	$\phi_{\text{outer}}$	$\phi_{\text{inner}}/\phi_{\text{outer}}$
SwB1	0.75	0.75	1
SwB5	1	0.5	2
SwB9	1.125	0.375	3

stratification systematically. The flames are stabilized by a recirculation zone created behind the bluff body. Velocity measurements are provided by Zhou et al. [59], and the temperature and mass fraction measurements are provided by Sweeney et al. [17,18].

The cylindrical computational domain spans 200 mm in the axial  $z$ -direction and 200 mm in the radial  $r$ -direction. The domain

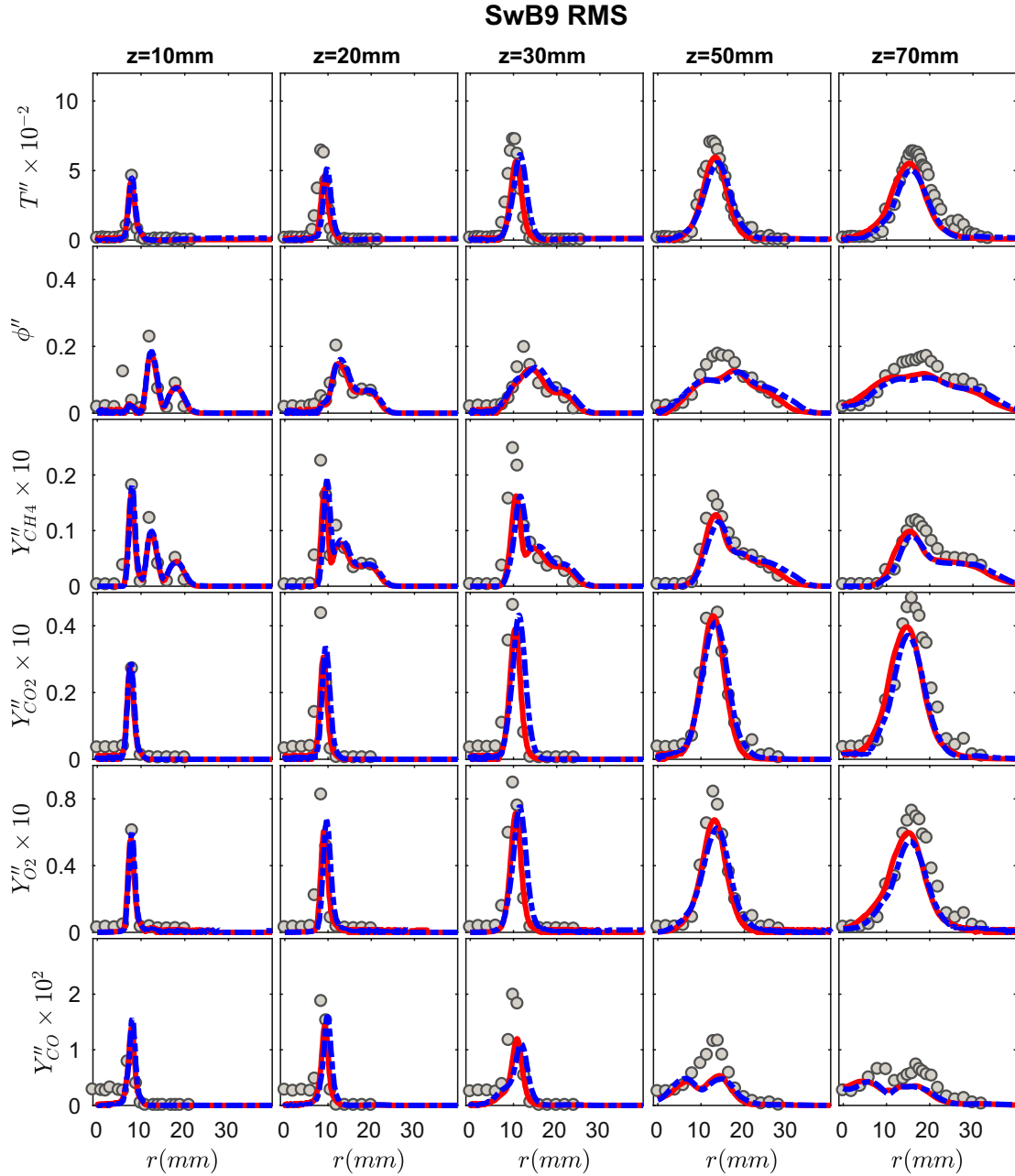


**Fig. 12.** SwB9: The radial profiles of the r.m.s. of temperature and the r.m.s. of mass fractions of  $\text{CH}_4$ ,  $\text{CO}_2$ ,  $\text{O}_2$  and  $\text{CO}$  at five axial locations of  $z = 10, 20, 30, 50, 70\text{mm}$ . Symbols: experimental data; red solid line: Model ED25; blue dot dashed line: Model DD25. (For interpretation of the references to color in this figure legend, the reader is referred to the web version of this article).

is discretized using a non-uniform  $192 \times 128 \times 96$  cylindrical grid. The grid is concentrated near the nozzle in the axial direction and in the shear layer between the fuel jets in the radial direction.

For the fuel jets, the instantaneous inlet velocities are obtained from two separate turbulent annular pipe simulations. A top-hat profile of  $0.4\text{ m/s}$  is specified for the air coflow. At the bluff body and the wall-lips, no-slip boundary conditions are applied. The adiabatic boundary condition is applied to the surface of the bluff body, and the heat loss through the bluff body is neglected. The zero-gradient boundary conditions are imposed for all the fields at the outlet and at the far field. Approximately 20 particles are employed per cell in the PDF solver. The methane/air combustion is represented by the augmented reduced mechanism (ARM1) [60]. An error tolerance  $\epsilon_{tol}$  of  $5 \times 10^{-5}$  is employed in ISAT and this error tolerance has been found to be sufficiently low to ensure

accurate solutions in similar simulations [39,43]. The simulations are parallelized using the domain decomposition technique with 192 cores. A constant time step of  $\Delta t = 4 \times 10^{-6}\text{ s}$  corresponding to a Courant number of approximately 0.2 is employed. The simulations are first performed for five flow-through times based on the inner fuel stream velocity to reach the statistically-stationary state, then another five flow-through times are performed to collect the statistics. The normalized computational cost is approximately  $380\ \mu\text{s}$  per grid cell per time step, and approximately 25536 h CPU-time is required to complete each simulation. In present study each simulation is parallelized using 192 cores, and is completed in approximately 5.5 days, which demonstrates the efficiency of the implementation of the LES/PDF method in *pdfFoam* solver. Three parametric models are considered in this study, as shown in Table 2. The differential diffusion effect described in Section 2.2 is included

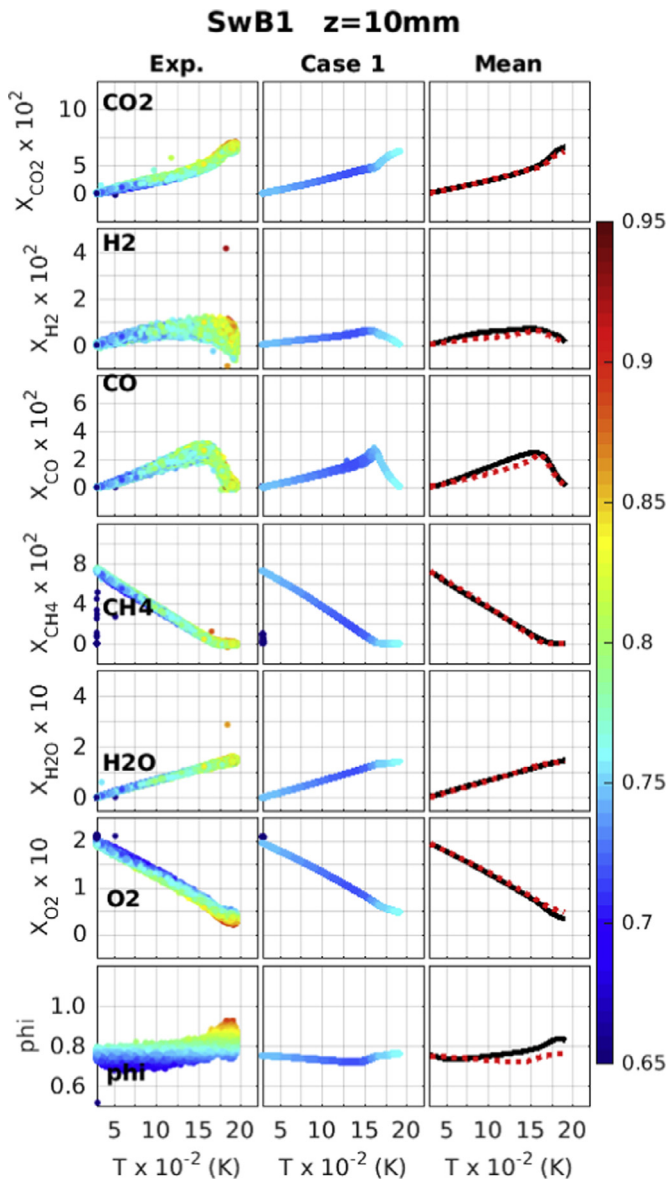


**Fig. 13.** SwB1: Scatter plots of mole fractions of  $\text{CO}_2$ ,  $\text{H}_2$ ,  $\text{CO}$ ,  $\text{CH}_4$ ,  $\text{H}_2\text{O}$ ,  $\text{O}_2$  and  $\phi$  as a function of temperature from LES/PDF simulation and experimental measurements at  $z = 10$  mm, color-coded by the equivalence ratio. Black solid line: conditional mean of species from experiment; red dashed line: conditional mean of species from simulation. (For interpretation of the references to color in this figure legend, the reader is referred to the web version of this article).

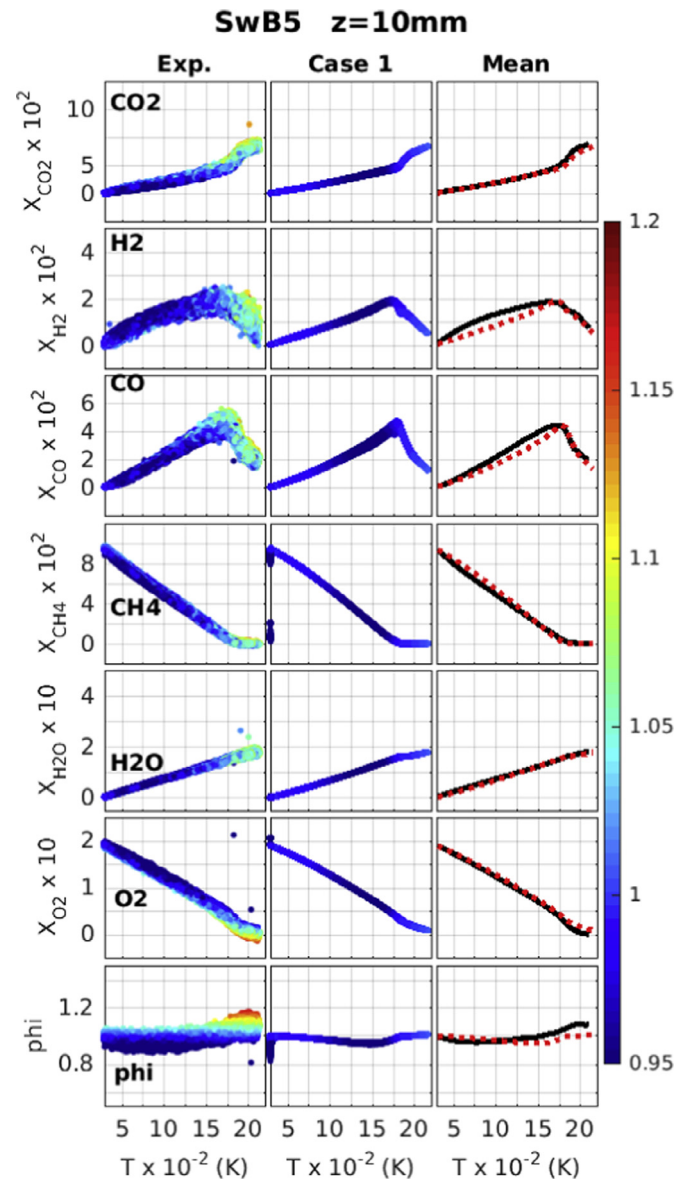


**Fig. 14.** SwB5: Scatter plots of mole fractions of  $\text{CO}_2$ ,  $\text{H}_2$ ,  $\text{CO}$ ,  $\text{CH}_4$ ,  $\text{H}_2\text{O}$ ,  $\text{O}_2$  and  $\phi$  as a function of temperature from the LES/PDF simulation and the experimental measurements at  $z = 10$  mm, color-coded by the equivalence ratio. Black solid line: conditional mean of species from experiment; red dashed line: conditional mean of species from simulation. (For interpretation of the references to color in this figure legend, the reader is referred to the web version of this article).

**Table 2**

Model variations for parametric studies.

Model	$C_m$ mixing coefficient	Differential diffusion	SwB1	SwB5	SwB9
DD25	25	✓	✓	✓	✓
DD50	50	✓	✗	✓	✗
ED25	25	✗	✓	✓	✓

in Models DD25 (baseline) and DD50, while the unity Lewis number assumption is applied to all species in Model ED25. Here, the ED model employs the unity Lewis number assumption in both molecular mixing and molecular transport, however, the DD model takes into account the differential diffusion in the molecular transport term while using the unity Lewis number assumption in molecular mixing term. The sensitivity of the results to  $C_m$  is investigated by comparing Models DD25 ( $C_m = 25$ ) and DD50

( $C_m = 50$ ). The effects of differential diffusion are studied by comparing Models DD25 and ED25. The simulations considered in the present study are summarized in Table 2. The models of DD25 and ED25 are applied to all stratified flames, while the model of DD50 is only applied to moderately stratified flame, SwB5.

#### 4. Results

In this section, the baseline numerical results are first validated through a hierarchical comparison with the experimental measurements, including the global characteristics (e.g., the lengths of the recirculation zones) in Section 4.1, radial profiles of mean and r.m.s. velocities in Section 4.2, radial profiles of mean and r.m.s. scalars in Section 4.3, and scatter plots of species in Section 4.4. Following the validation, the effect of stratification on the flame structure is discussed. The effect of differential

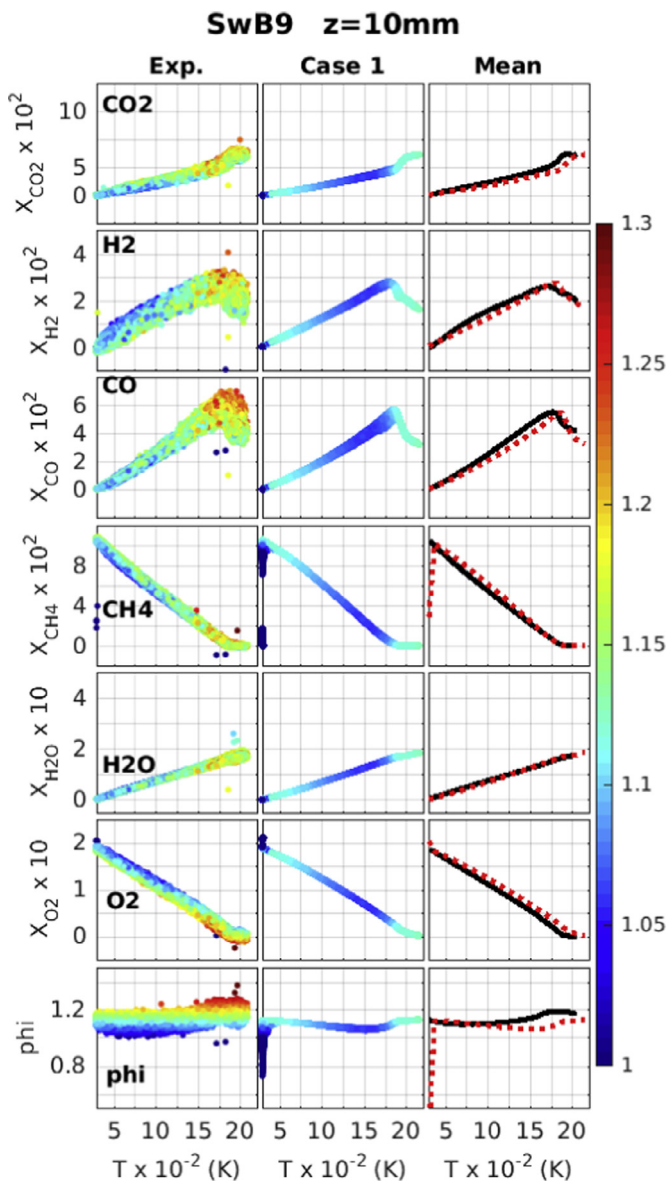


**Fig. 15.** SwB9: Scatter plots of mole fractions of  $\text{CO}_2$ ,  $\text{H}_2$ ,  $\text{CO}$ ,  $\text{CH}_4$ ,  $\text{H}_2\text{O}$ ,  $\text{O}_2$  and  $\phi$  as a function of temperature from the LES/PDF simulation and the experimental measurements at  $z = 10$  mm, color-coded by the equivalence ratio. Black solid line: conditional mean of species from experiment; red dashed line: conditional mean of species from simulation. (For interpretation of the references to color in this figure legend, the reader is referred to the web version of this article).

diffusion and the effect of the mixing rate parameter,  $C_m$ , are addressed last, through the parametric studies in Sections 4.6 and 4.7, respectively.

#### 4.1. The general behavior of the flames

The iso-contours of the mean equivalence ratio and the mean axial velocity superimposed by the mean streamlines from Model DD25 are presented in Fig. 2. Recirculation zones that are marked by the streamlines can be clearly observed behind the bluff body. Table 3 compares the lengths of the recirculation zones that are obtained from the simulations and from the experiments. The discrepancy between the baseline simulations (Model DD25) and the experiments is below 10% for all the cases. The trend of the variations in the length of recirculation zones is also consistently captured by the numerical results. The length of the recirculation zone

**Table 3**  
The length of recirculation zones (mm).

Case	DD25	ED25	DD50	Exp.
SwB1	23	23.25	–	24
SwB5	13.5	14	10	14.5
SwB9	14	14.5	–	15

in the premixed case, SwB1, is significantly longer than those in the stratified cases. Moreover, the length in SwB5 is slightly shorter than that in SwB9. Such variation can possibly be explained by the volume expansion rates within the recirculation zones, which will be further discussed in Section 4.7.

The flame fronts, defined as the loci of the peak r.m.s. temperature in the radial direction, are marked by the white and black points in Fig. 2 for the Models DD25 and DD50, respectively. The flame front in SwB1 is mainly located within the regions with uniform equivalence ratios, as shown in Fig. 2. Far downstream at approximately 50 mm, the flame front begins to encounter slight gradients of the equivalence ratio, due to the mixing between the fuel streams and the air coflow. For SwB5 and SwB9, the flame fronts start to propagate into regions much earlier with stratification, i.e., after approximately  $z = 20$  mm, due to the differences in equivalence ratios between the inner and outer jets. However, it should be emphasized that the flame fronts mainly propagate into uniform equivalence ratios within the recirculation zones behind the bluff body for all the cases.

#### 4.2. Velocities

The mean and r.m.s. of the resolved axial and radial velocities are examined in this section to further validate the model predictions. The radial profiles obtained from SwB1, SwB5 and SwB9 at four different axial locations are compared with the experimental measurements, as shown in Figs. 3–6. The mean resolved axial velocity profiles agree well with the experimental data. The mean resolved radial velocities show good consistency with the experimental data within the recirculation zone for all three cases SwB1, SwB5 and SwB9, as shown in Fig. 4. Deviations appear at further downstream locations. On the centerline, the simulations predict zero radial velocity, demonstrating axisymmetry. However, the experimental measurements show non-zero radial velocities on the centerline. These discrepancies have also been observed in the previous LES simulations [26,27], and they can be attributed to the asymmetric characteristics of this kind of burner. The profiles of the r.m.s. of the resolved axial velocities agree well with the experimental profiles for all three cases. Within the recirculation zone, the r.m.s. values are smaller than the experimental data. The r.m.s. radial velocities are slightly higher than the measurements at  $z = 30$  mm, and match reasonably well with the experimental measurements at other locations.

#### 4.3. Scalars

To further validate the simulations, the mean temperature  $T$ , equivalence ratio  $\phi$  and mass fractions  $Y$  of  $\text{CH}_4$ ,  $\text{CO}_2$ ,  $\text{O}_2$  and  $\text{CO}$  are compared with the experimental measurements at five different axial locations in Figs. 7–9. The mean temperature profiles are in very good agreement with the measurements for all the cases. For the cases of SwB5 and SwB9, the temperature in the recirculation zone is over predicted by approximately 100 K. The discrepancy can be attributed to the adiabatic assumption specified for the bluff body [31]. At axial locations  $z = 50$  and 70 mm, the temperature profiles for SwB1 are well-predicted, whereas, they have slight discrepancies for SwB5 and SwB9 at the same locations.

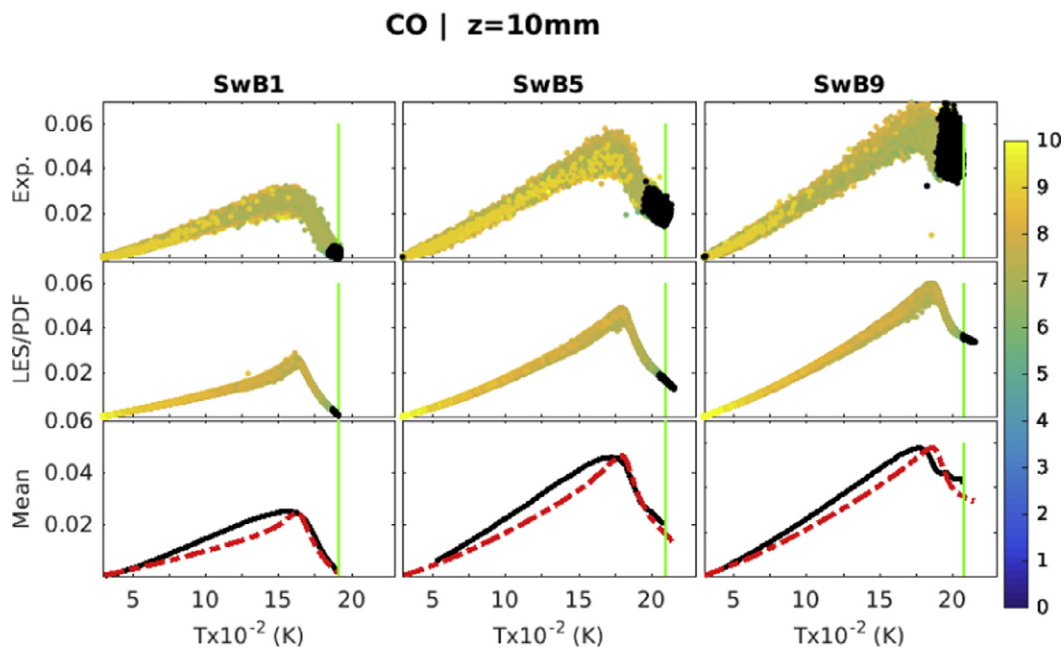


**Fig. 16.** Scatter plots of mass fractions of CO as a function of temperature obtained from the experimental measurements (top) and the LES/PDF simulation (middle) at  $z = 10$  mm, color-coded by the radial positions, and the mean conditional on temperature (bottom). The particles that are within the recirculation zones (i.e., radial locations smaller than 5 mm) are colored by black. Black solid line: conditional mean of species from the experiments; red dashed line: conditional means of species from the simulations. Green lines indicate the maximum temperature in the experimental data: 1920 K for SwB1; 2150 K for SwB5; 2080 K for SwB9. (For interpretation of the references to color in this figure legend, the reader is referred to the web version of this article).

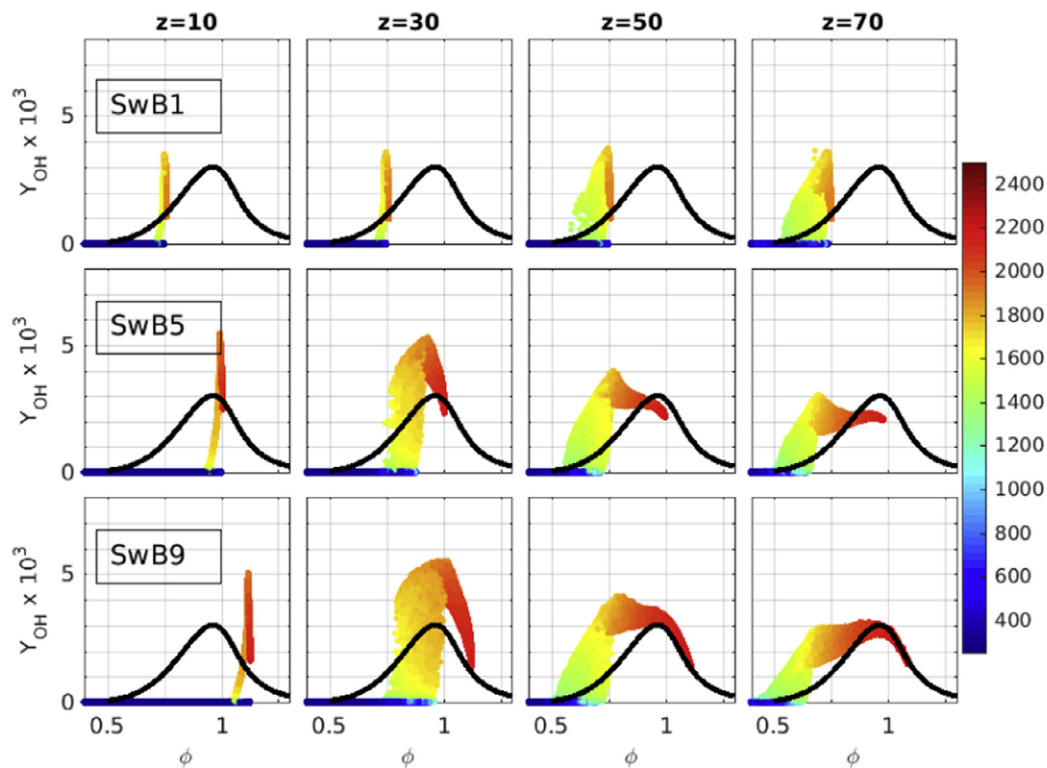


**Fig. 17.** Scatter plots of OH versus equivalence ratio, color-coded by temperature from LES/PDF simulations with Model DD25 for SwB1, SwB5 and SwB9 at  $z = 10, 30, 50, 70$  mm. Black solid line shows the OH as a function of the equivalence ratio obtained from the chemical equilibrium calculation.

The equivalence ratio profiles exhibit overall good agreement with the measurements for all the three cases. Similar to what is observed with the temperature profiles, small deviations exist at the locations of  $z = 50$  and  $70$  mm in SwB5 and SwB9. Close to the centerline, the equivalence ratios are slightly under-estimated. This could be explained by the under-predicted  $\text{CO}_2$  and the

over-predicted  $\text{O}_2$  profiles in the SwB1 case. For the SwB5 and SwB9 cases, the possible reason could be the under-estimated CO mass fractions.

The mean  $\text{CH}_4$  profiles are in good agreement with the measurements for all the three cases at all the axial locations. The  $\text{CO}_2$  and  $\text{O}_2$  profiles are well predicted in SwB5 and SwB9. However,

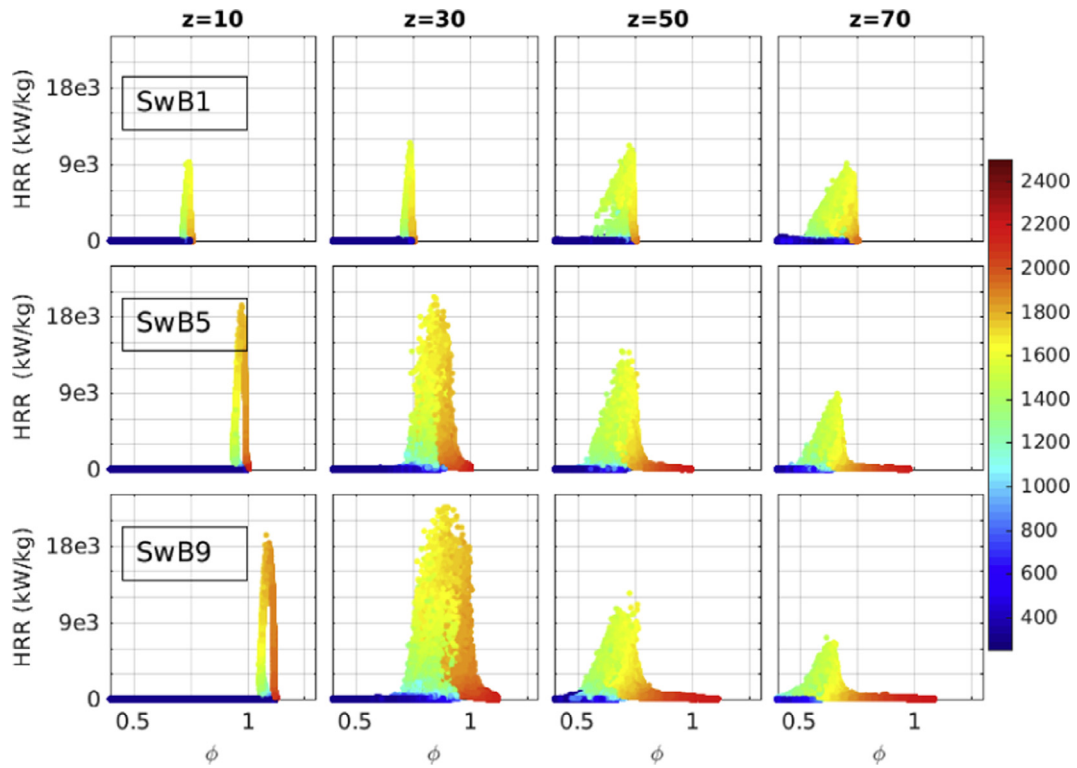


**Fig. 18.** Scatter plots of HRR versus equivalence ratio, color-coded by temperature from LES/PDF simulations with Model DD25 for SwB1, SwB5 and SwB9 at  $z = 10, 30, 50, 70$  mm.

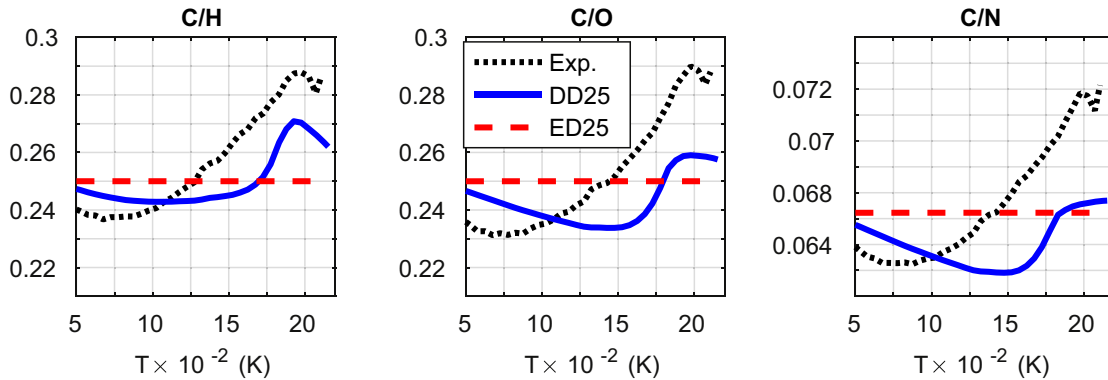


**Fig. 19.** The atom ratios C/H, C/O and C/N for the moderately stratified case, SwB5, obtained from the experiment, Model DD25 and Model ED25. Black dotted line: experimental data; red dashed line: Model ED25; blue solid line: Model DD25. (For interpretation of the references to color in this figure legend, the reader is referred to the web version of this article).

for SwB1,  $\text{CO}_2$  is slightly under-predicted and  $\text{O}_2$  is slightly over-predicted close to the centerline. For SwB5 and SwB9, the CO profiles are lower than the experimental measurements. Similar discrepancies in the CO profiles have also been observed in the previous LES studies of the same burner [26–28], as shown in Fig. 23. The discrepancies in the CO profiles can be attributed to the over-estimated temperature, which will be further addressed in Section 4.4. It should be noted that the CO concentration is much higher in SwB5 and SwB9, than that in SwB1. This could be due to the higher equivalence ratios in the stratified cases within the recirculation zones, such that more CO can be converted into  $\text{CO}_2$  by the excess oxygen in the premixed case.

The total r.m.s. of temperature, equivalence ratio and the mass fractions of  $\text{CH}_4$ ,  $\text{CO}_2$ ,  $\text{O}_2$  and CO profiles are presented in Figs. 10–12, and compared with the measurements. The total r.m.s. of the scalars are defined as  $Y_{\alpha,rms} = (\langle Y_{\alpha}^2 \rangle - \langle \tilde{Y}_{\alpha} \rangle^2)^{1/2}$  where  $\langle \cdot \rangle$

denotes the time averaging. All the profiles are overall in good agreement with the measurements. At axial locations of  $z = 50$  and  $70$  mm, the fluctuations are slightly lower than those obtained from the measurements but the trends in the experimental data are well captured at these locations. Moreover, for all three cases, SwB1, SwB5 and SwB9, within the recirculation zone, the r.m.s. profiles of all scalars are smaller than the measurements. Similar discrepancies have also been reported in the previous LES simulations [26–28], as shown in Fig. 24. The differences can be partially attributed to the over-predicted relaminarization effects within the high-temperature recirculation zones [27].

#### 4.4. Scatter plots

To further understand the discrepancy observed in the mean and r.m.s. profiles, the scatter plots of the mole fractions of all the

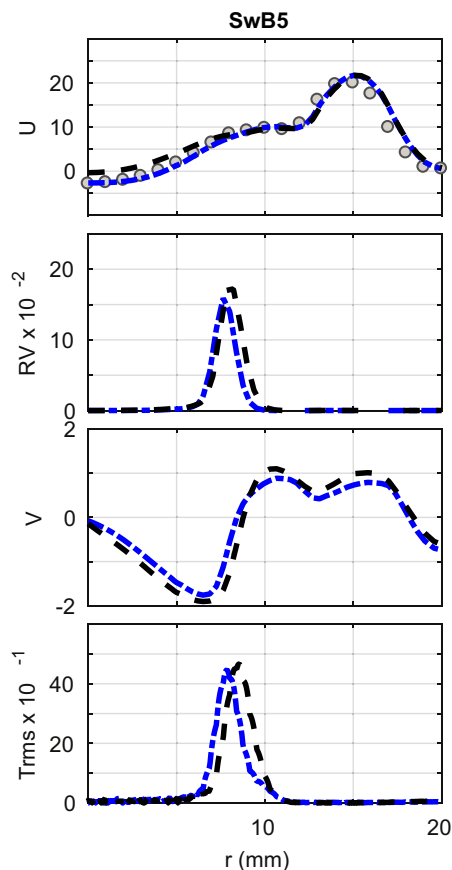


**Fig. 20.** The radial profile of the mean axial velocity, the mean rate of change of specific volume due to mixing and reacting (RV), the mean radial velocity, the r.m.s. temperature for the moderately stratified flame, SwB5, at  $z = 10$  mm. The blue dot dashed line: the results with Model DD25; the black dashed line: the results with Model DD50; the symbols: the experimental data. (For interpretation of the references to color in this figure legend, the reader is referred to the web version of this article)

experimentally measured species,  $\text{CO}_2$ ,  $\text{H}_2$ ,  $\text{CO}$ ,  $\text{CH}_4$ ,  $\text{H}_2\text{O}$ ,  $\text{O}_2$ , and the equivalence ratio,  $\phi$ , are presented in the temperature space at  $z = 10$  mm, as shown in Figs. 13–15. The mean conditional on temperature,  $\langle X_\alpha | T \rangle$ , obtained from the simulations are also compared with the experimental data. The plots are color-coded by the equivalence ratio. The scatter plots are generated using the notional Lagrangian particles from five different time steps. The scatter plots from the LES/PDF simulations are in good agreement with the experimental data. The plots from the simulations are slightly narrower in the temperature space than those in the experimental measurements, however the trends of all species are well captured. The conditional means from the simulations are in good agreement with those from the experimental data. The conditional means of  $\text{H}_2$  and  $\text{CO}$  are slightly underestimated for temperature lower than approximately 1750 K, while the conditional means of  $\text{O}_2$  are slightly overestimated for temperature higher than this value. Considering the good consistency observed for the other species, the discrepancy in the conditional mean of the equivalence ratio can be attributed to the discrepancies in  $\text{H}_2$  and  $\text{CO}$  mole fractions for temperature lower than approximately 1750 K, and to discrepancy in  $\text{O}_2$  for temperature higher than this value.

To map the behavior in the composition space to the physical space, the scatter plots of the mass fraction of  $\text{CO}$  as a function of temperature are color-coded by the radial positions at  $z = 10$  mm for SwB1, SwB5 and SwB9, as presented in Fig. 16. The points with radial locations smaller than 5 mm are colored by black to high-

light the points close to the centerline. As observed in the previous section, the conditional means of  $\text{CO}$  are underestimated when the temperature is lower than approximately 1750 K, and they are well predicted when the temperature is higher than 1750 K. The maximum temperature occurs near the centerline within the recirculation zones for all three cases, as depicted by the black points. For temperature greater than 1750 K, the mass fractions of  $\text{CO}$  decrease with increasing temperature, and clearly the under-predicted  $\text{CO}$  mass fractions are correlated with the over-predicted temperatures within the recirculation zones. Beyond the peak temperature measured in the experiments, the predicted conditional mean mass fractions in Fig. 16 extend along their existing manifolds in the composition space, into regions with higher temperatures. Mercier et al. [31] have shown that the non-adiabatic boundary conditions specified on the bluff body surface can significantly improve the temperature prediction for the stratified cases. Following the discussions above, the non-adiabatic temperature boundary condition is expected to improve the prediction of the  $\text{CO}$  mass fractions within the recirculation zones for the stratified cases.

#### 4.5. Effects of stratification

With the comprehensively validated numerical results presented in the previous subsections, the detailed flame structures are examined in this section, leveraging the information provided by the notional Lagrangian particles. The effect of the stratification on the flame structure is first investigated in this section, by examining the distribution of  $\text{OH}$  and the heat release rate (HRR) in the equivalence ratio space.

The scatter plots of  $\text{OH}$  versus the equivalence ratio are shown in Fig. 17 at four different axial locations of  $z = 10, 30, 50, 70$  mm. These axial locations are selected to examine the  $\text{OH}$  distribution when the fuel-air mixture from the inner jet mixes progressively with the mixtures from the outer jet and from the air coflow. At  $z = 10$  mm,  $\text{OH}$  mass fractions vary within a very thin zone in the equivalence ratio space, indicating a purely premixed combustion mode for all three cases. At  $z = 30$  mm, the distribution of  $\text{OH}$  mass fractions still demonstrates a premixed combustion mode for SwB1, and the stratification in the equivalence ratio space is clearly observed for SwB5 and SwB9. At  $z = 50$  mm, a significant amount of  $\text{OH}$  is observed at lower equivalence ratio for all the three cases, due to the mixing between the premixed jets and the air coflow. Meanwhile, between  $\phi = 0.75$  and the maximum equivalence ratio, the scatter plots begin to relax towards an equilibrium for SwB5 and SwB9, as indicated by the black solid line in Fig. 17. Finally the peak of  $\text{OH}$  mass fractions decreases downstream for SwB5 and SwB9, and maintains constant for SwB1. The evolution of the stratified flames clearly demonstrates the mixed-mode combustion behavior in the stratified flames.

The scatter plot of HRR calculated from the compositions and temperature versus equivalence ratio are presented in Fig. 18. The HRR scatter plots follow similar trends as the  $\text{OH}$  scatter plots in terms of the evolution of the distribution. Interestingly, the maxima of HRR are located at the location of  $z = 30$  mm for all three cases. The magnitudes of HRR are significantly reduced towards downstream locations for SwB5 and SwB9. For the stratified cases, the peak HRR is reduced to approximately 40% of the peak HRR calculated at the location of  $z = 30$  mm. Compared to SwB1, the heat release is taking place in a more distributed manner for the stratified flames.

#### 4.6. Effect of differential diffusion

In this section, the effect of differential diffusion is examined by comparing the results from Models DD25 and ED25. The length of the recirculation zones in the simulations with Model DD25 are

slightly shorter than those with Model ED25 as given in Table 3. Consequently, the mean and r.m.s. velocity profiles from Models DD25 and ED25 have slight differences close to the centerline. The mean and r.m.s. scalar profiles from Models DD25 and ED25 are very close to one another for SwB1, SwB5 and SwB9 at all axial locations, as shown in Figs. 7–12.

The effect of the differential diffusion has been experimentally examined by Barlow et al. [21] using the Cambridge/Sandia swirl burner. There the atom ratios of C/H, C/O, and C/N are not conserved going from reactants to products across the flame brush, and differential diffusion was proposed to be the possible cause. To examine this hypothesis, the atom ratios C/H, C/O and C/N for the moderately stratified case, SwB5, obtained from Models DD25 and ED25 are compared with one another as well as with those reconstructed from the scatter experimental data at the axial location of  $z = 10$  mm in Fig. 19. While the atom ratios in Model ED25 remain constant across flame front, Model DD25 displays variation of the atom ratios as a function of temperature, which supports the hypothesis by Barlow et al. [21]. Although the trends in Fig. 19 agree well with those obtained from the experiments, the magnitudes of the variation are under-predicted by the numerical results. Such discrepancy can be partly attributed to the modeling approach adopted in this study. Here, the differential diffusivity is only incorporated through the spatial transport by molecular diffusion, modeled by the mean drift term in Eq. (7). The unity Lewis number assumption is still employed for all species in the mixing frequency model (Eq. (9)) used in the IEM mixing model. The DNS studies [61,62] have shown that wide discrepancies may occur among species mixing frequencies. Richardson and Chen [63] proposed a model to account for the differential diffusion effect through individual mixing frequencies for different species, which will be incorporated in future work.

#### 4.7. Effect of the mixing parameter $C_m$

As one of the key modeling parameters, the effect of the mixing rate parameter  $C_m$  is investigated by comparing the results obtained from Models DD25 and DD50 for SwB5. The length of the recirculation zone, as given in Table 3, is predicted to be shorter for Model DD50 than that for Model DD25. Additionally, the flame fronts in Model DD50 denoted by black points in Fig. 2 are slightly shifted outward in the radial direction compared to those obtained from Model DD25 denoted by white points. Due to these differences in the flame structure, apparent shift in the physical space is observed in the the mean and r.m.s. profiles of velocity and scalar between Model DD25 and Model DD50, as shown in Figs. 3–12.

To further understand how the mixing frequency  $C_m$  alters the flame structure, Figure 20 shows the mean axial and radial velocities, the mean rate of change of the specific volume due to mixing and reaction (RV), and the r.m.s. temperature profiles for SwB5, at  $z = 10$  mm. The r.m.s. temperature profiles locate the flame fronts, where the specific volume reaches its maximum expansion rates. The radial velocity crosses zero near the flame fronts. At the product side of the flame front, the radial velocity is negative (pointing towards the centerline), and is positive at the fresh mixture side. This suggests that the expanded volume in the flame zone pushes the products inward towards the centerline and pushes the fresh mixture outward. Higher values of the  $C_m$  coefficient result in higher mixing rates leading to higher volume expansion rate and higher radial velocities (in magnitude) in the vicinity of the flame fronts. The higher radial velocity directly leads to the reduction of the length of the recirculation zone. In addition, in Model DD25, the axial location of  $z = 10$  mm remains within the recirculation zone, while that location stays behind the recirculation zone in Model DD50. Consequently, Model DD25 predicts a negative axial velocity at  $z = 10$  mm, while Model DD50 gives a positive axial

velocity. As a conclusion, for bluff body stabilized premixed flames, the appropriate mixing rate has essential role to correctly predict the flame structures.

## 5. Conclusion

LES/PDF simulations of the Cambridge/Sandia stratified turbulent flames have been performed with finite-rate chemistry. The premixed (SwB1), the moderately stratified (SwB5) and the highly stratified (SwB9) flames are simulated using the same set of models and parameters. The length of the recirculation zone and the mean and r.m.s. velocity fields have been well predicted, using the baseline model parameters. The radial profiles of the mean and r.m.s. of temperature, equivalence ratio, and species mass fractions have been found to be in overall good agreement with the experimental measurements.

The scatter plots of species exhibit very good consistency with the measurements. The conditional means of species are also found to be in very good agreement with the experimental data. The scatter plots of OH and HRR demonstrate the evolution of flame structure in the equivalence ratio space at different axial locations. All three cases have exhibited premixed combustion mode close to the inlet, and the stratified combustion mode occurs at downstream locations due mainly to the mixing of fuel jets and the air coflow.

In the recirculation zone the temperature is slightly over-predicted while the CO mass fraction is under-predicted. The possible effect of the differential diffusion on these discrepancies has been examined. The results obtained with and without differential diffusion simulations show that the differential diffusion considered in the mean drift term has a negligible effect on the mean and r.m.s. profiles in all the cases of SwB1, SwB5 and SwB9. However, the variation of atom ratios in temperature space is qualitatively captured by the differential diffusion implementation, while no variation is predicted by the equal diffusivity model.

The effect of the mixing frequency parameter  $C_m$  has been also examined. It is found that increasing  $C_m$  reduces the length of the recirculation zone due to the increase in the volume expansion rate, and causes the flame front location to shift slightly in the radial direction. The shifting in the flame front location is found to have negligible effect on the flow fields under non-swirling conditions. However, it may have an important impact on the vortex breakdown that might occur under the swirl conditions.

The effect of the heat loss through the bluff body can lead to the under-prediction of the CO mass fractions within the recirculation zone, and such loss will be addressed in future work. Additionally, the effects of the swirl flow conditions are also under investigation.

## Acknowledgments

HT and XYZ are supported by the Donors of the American Chemical Society Petroleum Research Fund. HT and MM are grateful to the Scientific and Technical Research Council of Turkey (TUBITAK) for the support of this research through Grant 111M067 and 214M309, and Turkish Academy of Sciences (TUBA). This research at Cornell is funded by the U.S. Department of Energy, Office of Science, Office of Basic Energy Sciences under award number DEFG02-90 ER14128. The authors thank to Prof. Simone Hochgreb for providing for scatter plot measurements, and to Ji-Woong Park for the 1D laminar premixed flame calculations.

## Appendix A. The comparison with previous studies

In the literature, numerical studies of the Cambridge/Sandia turbulent stratified flame series under non-swirling condition have

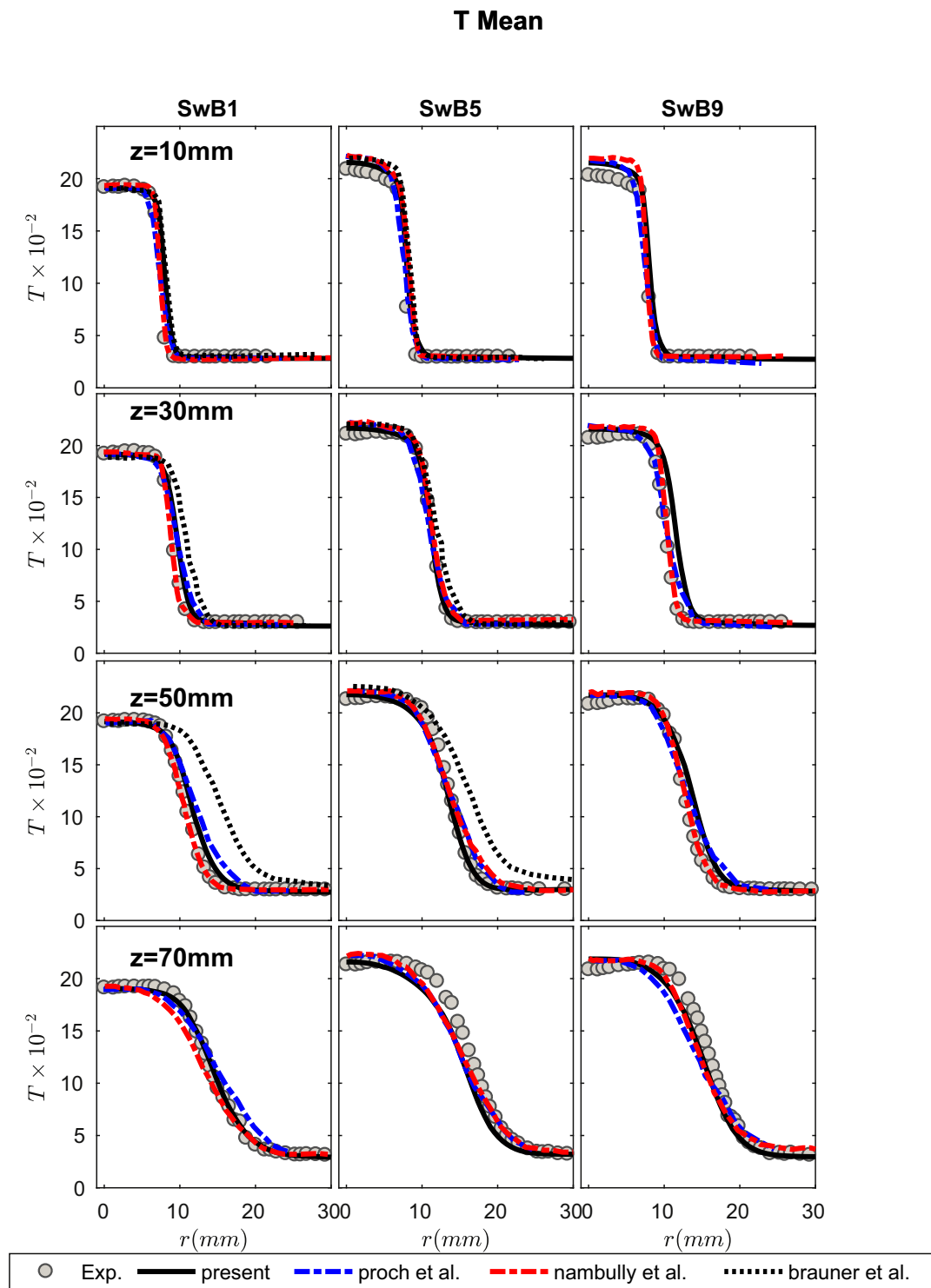


**Fig. 21.** The radial profile of the mean temperature at four different axial locations. The symbols: the experimental data; the black solid line: the present results with Case DD25; the blue dot dashed line: the results by Proch and Kempf [26]; the red dashed line: the results by Nambully et al. [27,30]; the black dashed line: the results by Brauner et al. [28]. (For interpretation of the references to color in this figure legend, the reader is referred to the web version of this article).

been performed using different combustion models in the LES context. These studies are summarized in Table 4. In this section, the mean and r.m.s. of temperature and the mass fraction of CO from different studies as well as the experimental data are compared.

The radial profiles of mean temperature from different studies are presented in Fig. 21. The results by Nambully et al. [27,30] and Proch and Kempf [26] are very close to the results in the present

study. However the results by Brauner et al. [28] have significant discrepancies downstream locations. In all the simulations the temperature are over estimated within the recirculation zone for the stratified flames, SwB5 and SwB9.

The r.m.s. of temperature are shown in Fig. 22. At upstream locations  $z = 10$  and  $30$  mm, the present results and the results by Brauner et al. [28] and Proch and Kempf [26] are

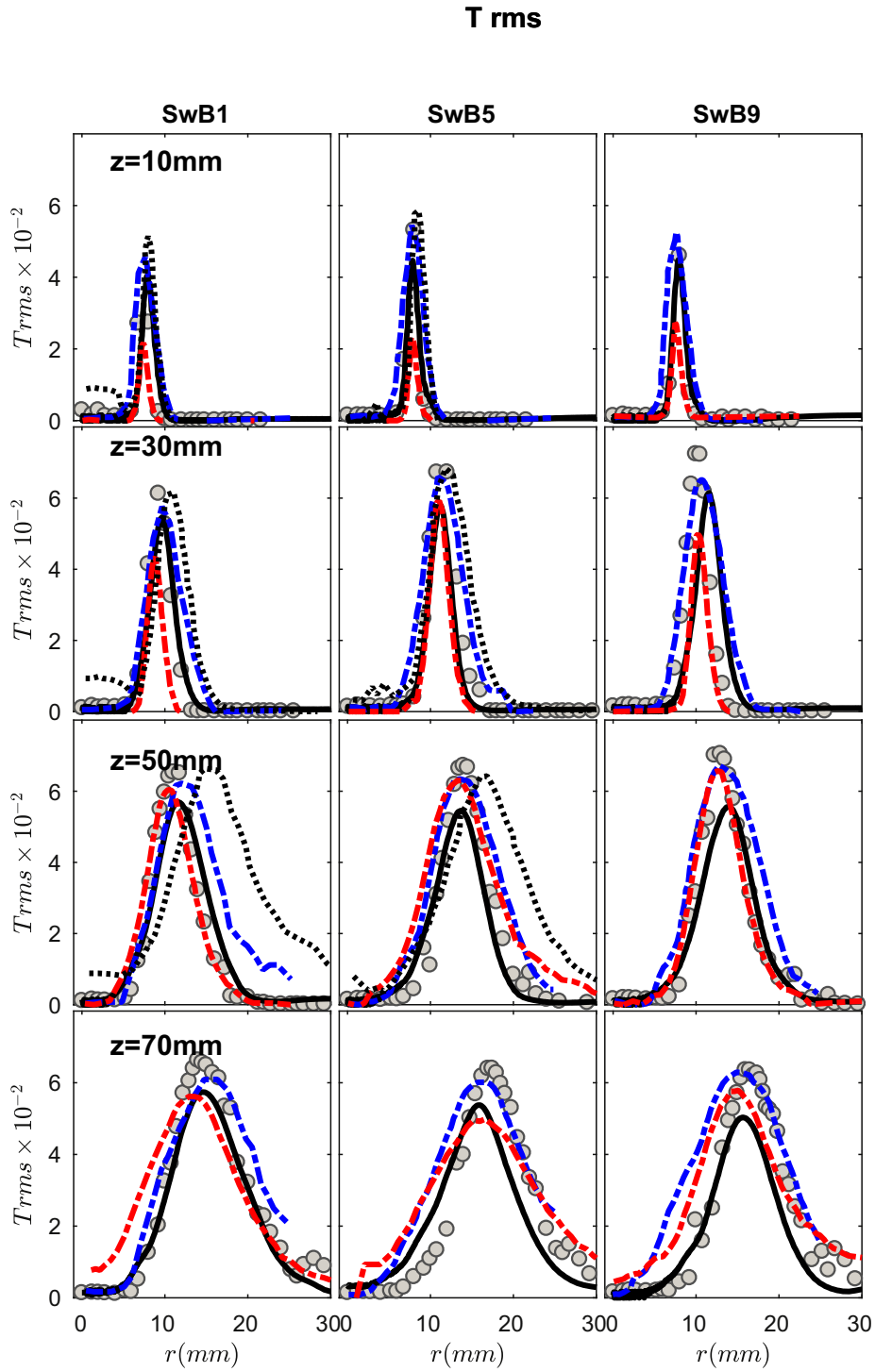


**Fig. 22.** The radial profile of the r.m.s. temperature at four different axial locations. The symbols: the experimental data; the black solid line: the present results with Case DD25; the blue dot dashed line: the results by Proch and Kempf [26]; the red dashed line: the results by Nambully et al. [27,30]; the black dashed line: the results by Brauner et al. [28]. (For interpretation of the references to color in this figure legend, the reader is referred to the web version of this article).

**Table 4**  
The numerical studies of the Cambridge/Sandia turbulent stratified flame.

Study	Model	Mesh size	Mechanism
Present	The transported PDF method based on Lagrangian Monte Carlo method	2.3 M	12-steps & 16-species
Proch et al. [26]	An artificially thickened flame model	100 M	GRI-3.0
Nambully et al. [27,30]	A filtered laminar flame PDF model	50 M	GRI-3.0
Brauner et al. [28]	The transported PDF method based on Eulerian stochastic field method	4 M	15-steps & 19-species

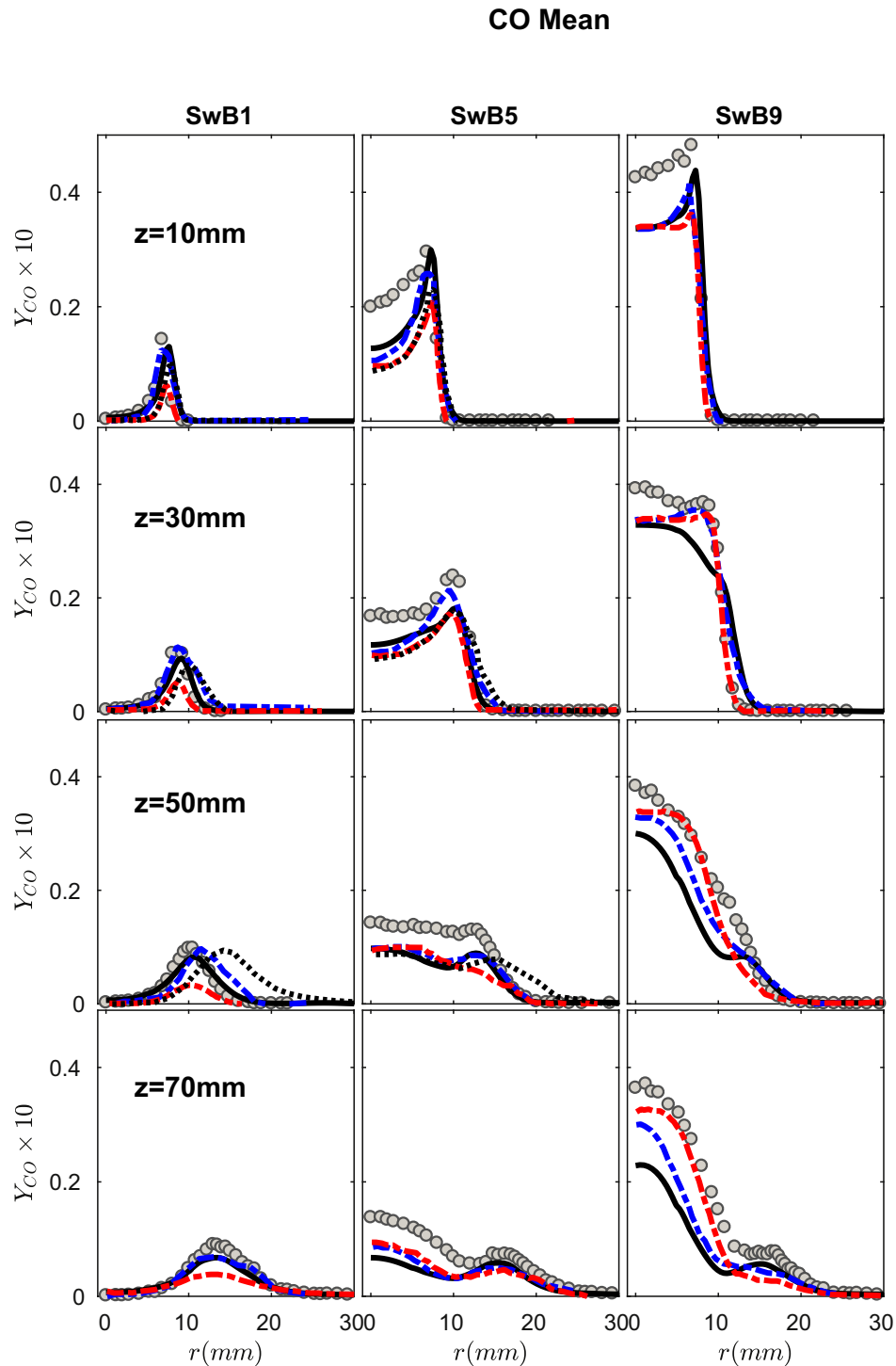


**Fig. 23.** The radial profile of the mean of the mass fraction of CO at four different axial locations. The symbols: the experimental data; the black solid line: the present results with Case DD25; the blue dot dashed line: the results by Proch and Kempf [26]; the red dashed line: the results by Nambully et al. [27,30]; the black dashed line: the results by Brauner et al. [28]. (For interpretation of the references to color in this figure legend, the reader is referred to the web version of this article).

similar to one another. However, the r.m.s temperature by Nambully et al. [27,30] are apparently under-estimated at those locations. At downstream locations of  $z = 50$  and  $70$  mm, the r.m.s. temperature profiles exhibit similar trends except the results by Brauner et al. [28], which are shifted outward in the radial direction.

The mean mass fraction of CO profiles are compared in Fig. 23. All the results are very close to one another. Interestingly, the discrepancies in the mass fraction of CO within the recirculation zone

for the stratified flames, SwB5 and SwB9 exist in all studies. For the highly stratified flame, SwB9, at downstream locations, the study by Nambully et al. [27,30] predicts better agreement with the experimental data than others.

The r.m.s. of the mass fraction of CO are shown in Fig. 24. The results by Proch and Kemp [26] have overall good agreement with the experimental data at all the axial locations for the premixed and stratified flames. The present results are slightly smaller than the results by Proch and Kemp [26], but the trends in the both

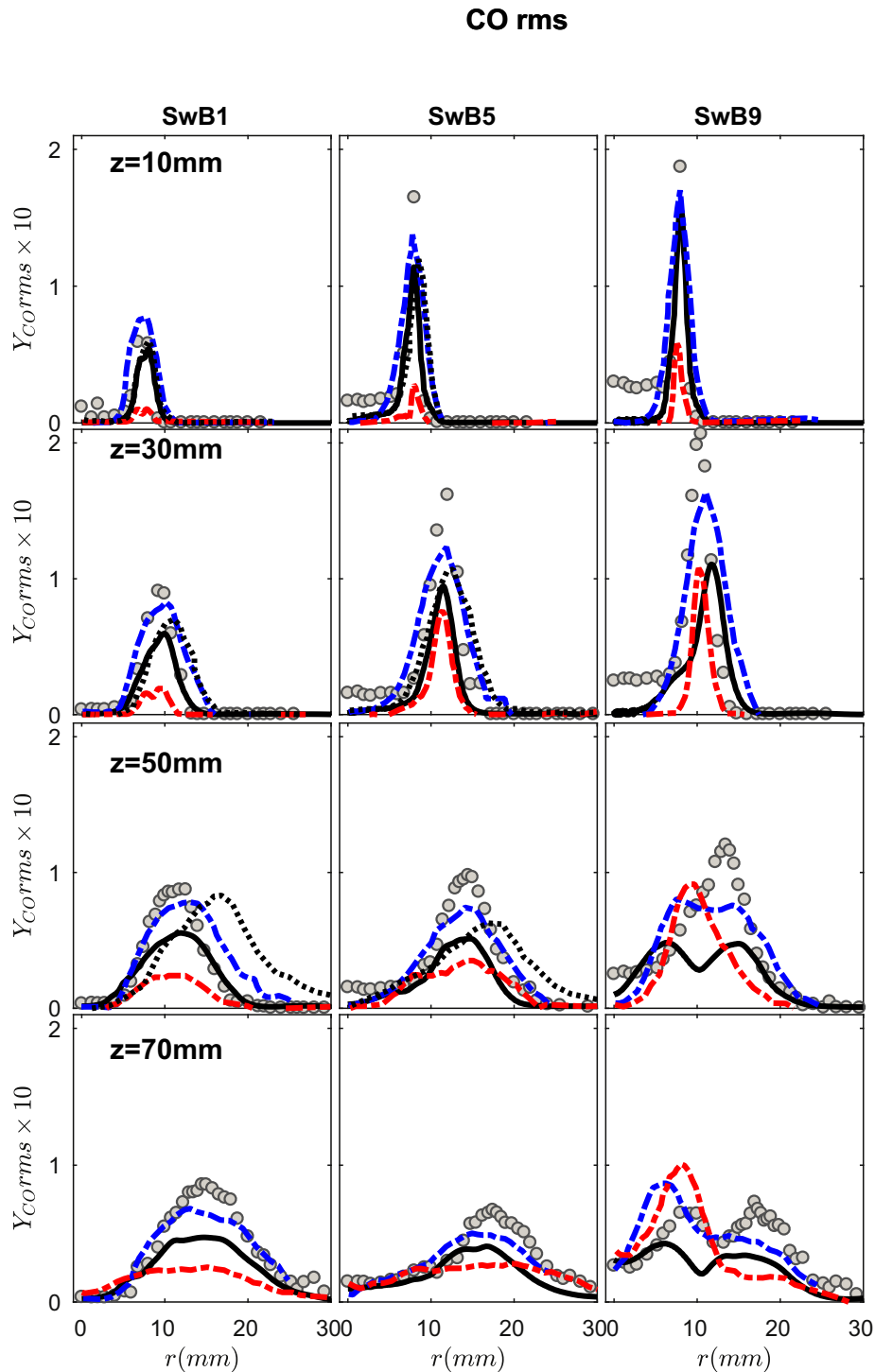


**Fig. 24.** The radial profile of the r.m.s. of the mass fraction of CO at four different axial locations. The symbols: the experimental data; the black solid line: the present results with Case DD25; the blue dot dashed line: the results by Proch and Kempf [26]; the red dashed line: the results by Nambully et al. [27,30]; the black dashed line: the results by Brauner et al. [28]. (For interpretation of the references to color in this figure legend, the reader is referred to the web version of this article).

studies are very similar. The study by Brauner et al. [27,30] has good prediction at the upstream locations, but they shifted outward in the radial direction at the downstream locations. Interestingly, the study by Nambully et al. [27,30] has very good agreement with the experimental data at the downstream location, while it suffers significantly from discrepancies at axial location  $z = 10$  mm.

In all the studies, the mean and r.m.s. of temperature and CO have very similar trends. Particularly, the over-prediction of mean

temperature and the under-prediction of mean CO close to the centerline for the stratified cases, SwB5 and SwB9 are exhibited in all the studies.

#### Appendix B. The sensitivity of equivalence ratio to $O_2$ concentration

As discussed before, the discrepancies in the equivalence ratio at high temperature could be due to the discrepancy in the

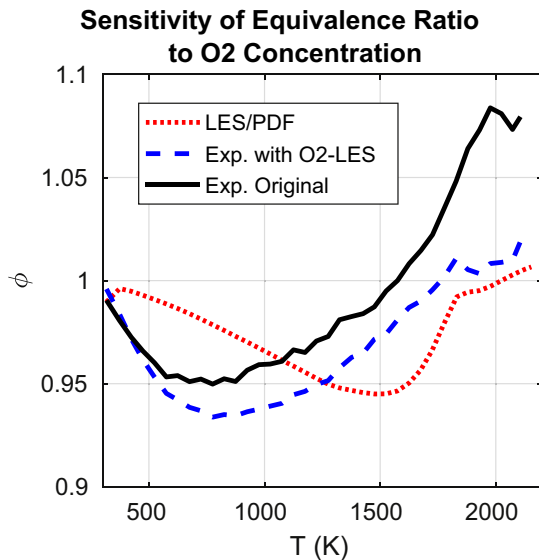


**Fig. 25.** The equivalence ratios versus temperature from the moderately stratified flame, SwB5 at axial location  $z = 10$  mm. The black solid line: the experimental data; the blue dashed line: the experimental data with  $O_2$  obtained from the LES/PDF simulation; the red dot dashed line: LES/PDF simulation. (For interpretation of the references to color in this figure legend, the reader is referred to the web version of this article).

$O_2$  concentration. To better understand this effect, we calculate an equivalence ratio using mole fraction from the experimental data except for the mole fraction of  $O_2$  that is obtained from the LES/PDF simulations.

The three equivalence ratios are compared in Fig 25. Here, we are mainly interested in the discrepancies at temperatures above 1750 K, which corresponds to the temperature in the recirculation zone. The equivalence ratio calculated using the  $O_2$  concentration from the LES/PDF calculation is much closer to the equivalence ratio obtained from the experiments, compared to that obtained directly from the LES/PDF calculation. As a conclusion, the equivalence ratio calculated using the mole fractions of  $CO_2$ ,  $H_2$ ,  $CO$ ,  $CH_4$ ,  $H_2$  and  $O_2$ , exhibits strong sensitivity to  $O_2$  concentration. Therefore, an accurate prediction/measurement of  $O_2$  is crucially important in for obtaining good agreement between the experimental measurements and numerical calculations.

## References

- [1] A.H. Lefebvre, Gas turbine combustion, CRC Press, Boca Raton (Florida), 1998.
- [2] Y. Takagi, A new era in spark-ignition engines featuring high-pressure direct injection, Symposium (international) on combustion, 27, Elsevier (1998), pp. 2055–2068.
- [3] P. Girard, M. Huneau, C. Rabasse, J. Leyer, Flame propagation through unconfined and confined hemispherical stratified gaseous mixtures, Symposium (international) on combustion, 17, Elsevier (1979), pp. 1247–1255.
- [4] N. Ishikawa, A diffusion combustor and methane-air flame propagation in concentration gradient fields, Combust. Sci Technol. 30 (1–6) (1983) 185–203.
- [5] J.A. Wehrmeyer, Z. Cheng, D.M. Mosbacher, R.W. Pitz, R. Osborne, Opposed jet flames of lean or rich premixed propane-air reactants versus hot products, Combust. Flame 128 (3) (2002) 232–241.
- [6] Y.M. Marzouk, A.F. Ghoniem, H.N. Najm, Dynamic response of strained premixed flames to equivalence ratio gradients, Proc. Combust. Inst. 28 (2) (2000) 1859–1866.
- [7] R. Lauvergne, F.N. Egolfopoulos, Unsteady response of  $C_3H_3$ /air laminar premixed flames submitted to mixture composition oscillations, Proc. Combust. Inst. 28 (2) (2000) 1841–1850.
- [8] B. Renou, E. Samson, A. Boukhalfa, An experimental study of freely propagating turbulent propane/air flames in stratified inhomogeneous mixtures, Combust. Sci. Technol. 176 (11) (2004) 1867–1890.
- [9] N. Pasquier, B. Lecordier, M. Trinite, A. Cessou, An experimental investigation of flame propagation through a turbulent stratified mixture, Proc. Combust. Inst. 31 (1) (2007) 1567–1574.

- [10] V. Robin, A. Mura, M. Champion, O. Degardin, B. Renou, M. Boukhalfa, Experimental and numerical analysis of stratified turbulent V-shaped flames, Combust. Flame 153 (1–2) (2008) 288–315.
- [11] P. Anselmo-Filho, S. Hochgreb, R.S. Barlow, R.S. Cant, Experimental measurements of geometric properties of turbulent stratified flames, Proc. Combust. Inst. 32 (2) (2009) 1763–1770.
- [12] B. Coriton, J.H. Frank, A.G. Hsu, M.D. Smooke, A. Gomez, Effect of quenching of the oxidation layer in highly turbulent counterflow premixed flames, Proc. Combust. Inst. 33 (1) (2011) 1647–1654.
- [13] M. Besson, P. Bruel, J. Champion, B. Deshaies, Inert and combusting flows developing over a plane symmetric expansion-experimental analysis of the main flow characteristics, 37th Aerospace Sciences Meeting and Exhibit (1999), p. 412.
- [14] M.S. Mansour, A study of turbulent partially premixed flames based on simultaneous imaging of velocity field and OH radical, Combust. Sci. Technol. 174 (2) (2002) 47–78.
- [15] F. Seffrin, F. Fuest, D. Geyer, A. Dreizler, Flow field studies of a new series of turbulent premixed stratified flames, Combust. Flame 157 (2) (2010) 384–396.
- [16] B. Böhm, J.H. Frank, A. Dreizler, Temperature and mixing field measurements in stratified lean premixed turbulent flames, Proc. Combust. Inst. 33 (1) (2011) 1583–1590.
- [17] M.S. Sweeney, S. Hochgreb, M.J. Dunn, R.S. Barlow, The structure of turbulent stratified and premixed methane/air flames I: Non-swirling flows, Combust. Flame 159 (9) (2012a) 2896–2911.
- [18] M.S. Sweeney, S. Hochgreb, M.J. Dunn, R.S. Barlow, The structure of turbulent stratified and premixed methane/air flames II: swirling flows, Combust. Flame 159 (9) (2012b) 2912–2929.
- [19] T. Kang, D. Kyritsis, Theoretical investigation of flame propagation through compositionally stratified methane-air mixtures, Combust. Theory Model. 13 (4) (2009) 705–719.
- [20] A.N. Lipatnikov, Stratified turbulent flames: recent advances in understanding the influence of mixture inhomogeneities on premixed combustion and modeling challenges, Progr. Energy Combust. Sci. 62 (2017) 87–132.
- [21] R.S. Barlow, M.J. Dunn, M.S. Sweeney, S. Hochgreb, Effects of preferential transport in turbulent bluff-body-stabilized lean premixed  $CH_4$ /air flames, Combust. Flame 159 (8) (2012) 2563–2575.
- [22] G. Kuenne, F. Seffrin, F. Fuest, T. Stahler, A. Ketelheun, D. Geyer, J. Janicka, A. Dreizler, Experimental and numerical analysis of a lean premixed stratified burner using 1D Raman/Rayleigh scattering and large eddy simulation, Combust. Flame 159 (8) (2012) 2669–2689.
- [23] A. Ketelheun, G. Kuenne, J. Janicka, Heat transfer modeling in the context of large eddy simulation of premixed combustion with tabulated chemistry, Flow Turbul. Combust. 91 (4) (2013) 867–893.
- [24] P. Trisjono, K. Kleinheinz, H. Pitsch, S. Kang, Large eddy simulation of stratified and sheared flames of a premixed turbulent stratified flame burner using a flamelet model with heat loss, Flow Turbul. Combust. 92 (1–2) (2014) 201–235.
- [25] F.C. Marincola, T. Ma, A. Kempf, Large eddy simulations of the Darmstadt turbulent stratified flame series, Proc. Combust. Inst. 34 (1) (2013) 1307–1315.
- [26] F. Proch, A.M. Kempf, Numerical analysis of the Cambridge stratified flame series using artificial thickened flame LES with tabulated premixed flame chemistry, Combust. Flame 161 (10) (2014) 2627–2646.
- [27] S. Nambully, P. Domingo, V. Moureau, L. Vervisch, A filtered-laminar-flame PDF sub-grid-scale closure for LES of premixed turbulent flames: II. Application to a stratified bluff-body burner, Combust. Flame 161 (7) (2014) 1775–1791.
- [28] T. Brauner, W. Jones, A. Marquis, LES of the Cambridge stratified swirl burner using a sub-grid PDF approach, Flow Turbul. Combust. 96 (4) (2016) 965–985.
- [29] A.R. Masri, Partial premixing and stratification in turbulent flames, Proc. Combust. Inst. 32 (2) (2015) 1115–1136.
- [30] S. Nambully, P. Domingo, V. Moureau, L. Vervisch, A filtered-laminar-flame PDF sub-grid scale closure for LES of premixed turbulent flames. Part I: formalism and application to a bluff-body burner with differential diffusion, Combust. Flame 161 (7) (2014) 1756–1774.
- [31] R. Mercier, T. Schmitt, D. Veynante, B. Fiorina, The influence of combustion SGS submodels on the resolved flame propagation. application to the LES of the Cambridge stratified flames, Proc. Combust. Inst. 35 (2) (2015) 1259–1267.
- [32] F. Proch, P. Domingo, L. Vervisch, A.M. Kempf, Flame resolved simulation of a turbulent premixed bluff-body burner experiment. Part I: analysis of the reaction zone dynamics with tabulated chemistry, Combust. Flame 180 (2017) 321–339.
- [33] J. Xu, S.B. Pope, PDF calculations of turbulent nonpremixed flames with local extinction, Combust. Flame 123 (3) (2000) 281–307.
- [34] M. Muradoglu, K. Liu, S.B. Pope, PDF modeling of a bluff-body stabilized turbulent flame, Combust. Flame 132 (1) (2003) 115–137.
- [35] R. Mokhtarpoor, H. Turkeri, M. Muradoglu, A new robust consistent hybrid finite-volume/particle method for solving the PDF model equations of turbulent reactive flows, Comput. Fluids 105 (2014) 39–57.
- [36] H. Wang, S.B. Pope, Large eddy simulation/probability density function modeling of a turbulent  $CH_4/H_2/N_2$  jet flame, Proc. Combust. Inst. 33 (1) (2011) 1319–1330.
- [37] R.R. Tirunagari, S.B. Pope, Characterization of extinction/reignition events in turbulent premixed counterflow flames using strain-rate analysis, Proc. Combust. Inst. 36 (2) (2017) 1919–1927.
- [38] R.R. Tirunagari, S.B. Pope, LES/PDF for premixed combustion in the DNS limit, Combust Theory Model 20 (5) (2016) 834–865.
- [39] J. Kim, S.B. Pope, Effects of combined dimension reduction and tabulation

- on the simulations of a turbulent premixed flame using a large-eddy simulation/probability density function method, *Combust. Theory Model.* 18 (3) (2014) 388–413.
- [40] M. Juddoo, A.R. Masri, S.B. Pope, Turbulent piloted partially-premixed flames with varying levels of O<sub>2</sub>/N<sub>2</sub>: Stability limits and PDF calculations, *Combust. Theory Model.* 15 (6) (2011) 773–793.
- [41] R. McDermott, S.B. Pope, A particle formulation for treating differential diffusion in filtered density function methods, *J. Comput. Phys.* 226 (2007) 947–993.
- [42] P.P. Popov, S.B. Pope, Large eddy simulation/probability density function simulations of bluff body stabilized flames, *Combust. Flame* 161 (12) (2014) 3100–3133.
- [43] R.R. Tirunagari, S.B. Pope, An investigation of turbulent premixed counterflow flames using large-eddy simulations and probability density function methods, *Combust. Flame* 166 (2016) 229–242.
- [44] W. Han, V. Raman, Z. Chen, LES/PDF modeling of autoignition in a lifted turbulent flame: analysis of flame sensitivity to differential diffusion and scalar mixing time-scale, *Combust. Flame* 171 (2016) 69–86.
- [45] P. Moin, K. Squires, W. Cabot, S. Lee, A dynamic sub-grid scale model for compressible turbulence and scalar transport, *Phys. Fluids A* 3 (1991) 2746–2757.
- [46] P.J. Colucci, F.A. Jaber, P. Givi, S.B. Pope, Filtered density function for large eddy simulation of turbulent reacting flows, *Phys. Fluids* 10 (1998) 499–515.
- [47] F.A. Jaber, P.J. Colucci, S. James, P. Givi, S.B. Pope, Filtered mass density function for large-eddy simulation of turbulent reacting flows, *J. Fluid Mech.* 401 (1999) 85–121.
- [48] H. Pitsch, H. Steiner, Large-eddy simulation of a turbulent piloted methane/air diffusion flame (Sandia Flame D), *Phys. Fluids* 12 (10) (2000) 2541–2554.
- [49] T.D. Dreben, S.B. Pope, Nonparametric estimation of mean fields with application to particle probability density function model for turbulent flows, Technical Report, Sibley School of Mechanical and Aerospace Engineering, Cornell University, Ithaca New York, 1992.
- [50] Y.Z. Zhang, D.C. Haworth, A general mass consistency algorithm for hybrid particle/finite-volume PDF methods, *J. Comput. Phys.* 194 (2004) 156–193.
- [51] P.P. Popov, H. Wang, S.B. Pope, Specific volume coupling and convergence properties in hybrid particle/finite volume algorithms for turbulent reactive flows, *J. Comput. Phys.* 294 (2015) 110–126.
- [52] H. Turkeri, S.B. Pope, M. Muradoglu, A LES/PDF simulator on block-structured meshes, *Combust. Theory Model.* (2018) 1–41.
- [53] P.L. Roe, Characteristic-based schemes for the Euler equations, *Ann. Rev. Fluid Mech.* 18 (1986) 337–365.
- [54] R.I. Issa, Solution of the implicitly discretized fluid flow equation by operator splitting, *J. Comput. Phys.* 62 (1986) 40–65.
- [55] H. Wang, P.P. Popov, S.B. Pope, Weak second order splitting schemes for Lagrangian Monte Carlo particle methods for the composition PDF/PDF transport equations, *J. Comput. Phys.* 229 (2010) 1852–1878.
- [56] S.B. Pope, Computationally efficient implementation of combustion chemistry using in situ adaptive tabulation, *Combust. Theory Model.* 1 (1997) 41–63.
- [57] L. Lu, S.R. Lantz, Z. Ren, S.B. Pope, Computationally efficient implementation of combustion chemistry in parallel PDF calculations, *J. Comput. Phys.* 28 (2009) 5490–5525.
- [58] H. Turkeri, X. Zhao, Large eddy simulation and probability density function modelling of swirling Cambridge/Sandia turbulent stratified flame series, 2018 ESSCI Spring Technical Meeting (2018).
- [59] R. Zhou, S. Balusamy, M.S. Sweeney, R.S. Barlow, S. Hochgreb, Flow field measurements of a series of turbulent premixed and stratified methane/air flames, *Combust. Flame* 160 (2012) 2017–2028.
- [60] C.J. Sung, C.K. Law, J.-Y. Chen, Augmented reduced mechanisms for NO emission in methane oxidation, *Combust. Flame* 125 (2001) 906–919.
- [61] E.R. Hawkes, R. Sankaran, J.C. Sutherland, J.H. Chen, Scalar mixing in direct numerical simulations of temporally evolving plane jet flames with skeletal CO/H<sub>2</sub> kinetics, *Proc. Combust. Inst.* 31 (1) (2007) 1633–1640.
- [62] E.S. Richardson, R. Sankaran, R.W. Grout, J.H. Chen, Numerical analysis of reaction-diffusion effects on species mixing rates in turbulent premixed methane-air combustion, *Combust. Flame* 157 (3) (2010) 506–515.
- [63] E.S. Richardson, J.H. Chen, Application of PDF mixing models to premixed flames with differential diffusion, *Combust. Flame* 159 (7) (2012) 2398–2414.